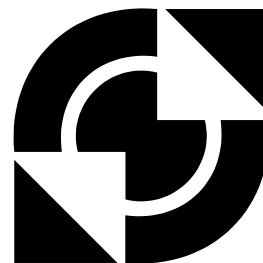


University of Twente

faculty of
chemical technology



Validation and verification of a discrete particle model in a pseudo 2D (spout-)fluid bed using pressures and digital images

D-colloquium Christiaan Zeilstra
26 april 2002
16:00
CT1814

D-commissie
voorzitter Prof. dr. ir. J.A.M. Kuipers
mentor Ir. J.M. Link
leden Dr. ir. A.G.J. van der Ham
Dr. ir. R. Stevens
Dr. ir. N.G. Deen



Enschede, april 2002

Abstract

The goal of this graduation project was the verification and validation of a discrete particle model in a pseudo 2D (spout-) fluid bed. Verification encompassed the ‘verification’ of the implementation of key model equations. These are the gas-solid drag equations and the gas-phase hydrodynamics.

Two gas-solid drag equations are present in the code. The Wen&Yu equation ($\varepsilon > 0.8$) and the Ergun equation ($\varepsilon < 0.8$). The Wen&Yu equation was verified using the terminal velocity of a falling particle. Both the Newton ($Re \geq 1000$) and intermediate region ($Re < 1000$) were properly implemented. The Newton region showed a deviation in the eventual terminal velocity of 0.024 % and the intermediate region one of 0.033 %. The Stokes region ($Re < 0.1$) showed a deviation of 2.47 %. This was caused by implementation of the Wen&Yu equations. If the Stokes equation was applied, a deviation of 0.048 % was found.

The Ergun equation was verified using the pressure drop over a packed bed. Deviations for superficial gas velocities of 1 m/s and 4 m/s were below 0.10 %. At 10 m/s, a deviation of 0.81 % was found.

The gas-phase hydrodynamics (Navier-Stokes equations) were verified by comparing the z-velocity profile from a simulation with the profile obtain from the analytical solution. It was found that the Navier-Stokes equations were properly implemented. Deviations were smaller than 0.5 % for the centre of the column. Near the walls, the deviation amounted up to 16 %, caused by the steep velocity gradient near the wall.

The validation was performed through experiments in the pseudo 2D (spout-) fluidised bed. Voidages were obtained through an imaging technique called bubble detection, particle fluxes through particle image velocimetry and pressure fluctuations from a high frequency pressure probe.

The voidage behaviour of the fluidisation and spout experiments compared with the simulations is usually within 0.05 voidage resemblance.

With the current camera equipment, particle image velocimetry could not be carried out for spout experiments and its application to normal fluidisation was also limited to cases with very low (near minimum fluidisation) superficial gas velocities.

Investigation of bedheight and pressure fluctuations using the high frequency pressure probe indicates that a direct coupling between these fluctuations exists. This goes for normal fluidisation as well as spout fluidisation.

The simulations accurately predicted the absolute pressure drop for normal fluidisation.

Voorwoord

Het Voorwoord. Door velen beschouwd als het meest gelezen deel van een afstudeerverslag. Waarschijnlijk hebben ze gelijk, ook al hoop ik dat de lezer van deze regels ook de hierop volgende paginas zal doornemen. Ik zal in ieder geval de lezer hiervoor warm proberen te maken door dit voorwoord zo te schrijven dat hij/zij de (lees)- smaak te pakken krijgt!

Het kiezen van De Opdracht. Na al een aantal enthousiaste AIO's bezocht te hebben was Jeroen Link de volgende te bezoeken potentiële werkgever. Uit het gesprek kwam al snel een aantal interessante punten na voren die de keuze voor deze opdracht niet moeilijk maakten. Jeroen had z'n eerste student binnengehaald.

De eerste werkdag werd besteed aan het installeren van het ons zo geliefde besturingssysteem Windows. Dit was een handeling die als een rode draad door de afstudeerperiode zou gaan en is als ik mij niet vergis toch zeker tien maal uitgevoerd in verschillende smaken en op minstens vijf verschillende computers.

Al gauw merkte ik dat de studentenzaal niet de oase van rust zou zijn die ik had verwacht. In het begin van het afstuderen waren het nog voornamelijk The Doors die met hun pingelorgeltje de deuren van AIO-kamers dicht konden krijgen, waarvan ik dacht dat ze altijd open zouden blijven. Later kwam daar nog een aantal andere verschijnselen bij. Uit de ene hoek werden partiële differentiaalvergelijkingen op zo'n wijze gepropagandeerd dat men bijna zou denken dat ze de oplossing voor een Midden-Oosten crisis zouden bevatten. Een andere hoek bevatte een felle tegenstander van commerciële software die geen moment ongebruikt liet om zijn 'superieure' besturingssysteem te promoten. Ondertussen werd door weer een ander te pas en te onpas snoepgoed aangeboden, terwijl ik van m'n tandarts nou juist te horen had gekregen dat dit toch heel erg verkeerd was. Kortom, het is eigenlijk een klein wonder dat dit verslag er nu toch ligt!

Nu we het toch over het verslag hebben; het zou niet tot stand gekomen zijn zonder waardevolle hulp van diverse mensen. Laat ik beginnen met de opstelling. In principe was de opstelling gebruiksklaar, maar enkele voorbereidende experimenten toonden aan dat dit jammerlijk genoeg toch niet het geval was. De technici werden ingeschakeld. Zij (en in het bijzonder Wim Leppink) konden na weken van noeste arbeid het bed met ballen op een zinvolle wijze in beweging krijgen.

Een werkende opstelling is niets zonder een goede data acquisitie. Het bleek nog een behoorlijke klus te zijn om de drukprobe werkende te krijgen, vooral om dat er nog geen werkend computerprogramma voor bestond. Robert Meijer en Martin van Sint Annaland worden bedankt voor de hulp bij het creëren van dit programma. De analyse van meetdata had ook nog een aantal voeten in de aarde. De PIV software was eerst een groot raadsel, hoewel dat misschien ook kwam door dat *andere* besturingssysteem. Gelukkig was Niels Deen zo vriendelijk om het besturingssysteem en de PIV software haarfijn uit te leggen en tevens te demonstreren. De resultaten van meetdata waren echter soms zo onduidelijk dat zelfs hij er geen pijn meer op kon trekken. Een speciaal woord van dank heeft echter Jeroen verdiend voor de vele uren die hij in de begeleiding heeft gestoken en voor de vele dingen die hij mij heeft geleerd over de code en fluidisatie in het algemeen.

Ik wil de vakgroep bedanken voor de gezellige koffiepauzes, lunchpauzes, borrels, vakgroepvolleybalwedstrijden en zelfs ski-vakanties. Last but not least wil ik mijn familie, vrienden en kennissen bedanken voor de support.

Christiaan

Table of contents

CHAPTER 1: INTRODUCTION	5
§1 PROJECT BACKGROUND	5
§2 INTRODUCTION TO FLUIDISATION	5
§2.1 <i>Regular fluidisation</i>	5
§2.2 <i>Spout fluidisation</i>	7
CHAPTER 2: THE MODEL.....	9
§1 THE DISCRETE PARTICLE MODEL	9
§1.1 <i>Introduction</i>	9
§1.2 <i>Multi-scale concept</i>	9
§1.3 <i>Discrete Particle Modelling</i>	10
§1.3.1 <i>Particle-particle interaction</i>	10
§1.3.2 <i>Gas-particle interaction</i>	12
§1.3.3 <i>Gas-phase Hydrodynamics</i>	13
§2 NUMERICAL IMPLEMENTATION.....	14
§2.1 <i>Division of bed in computational cells</i>	14
§2.2 <i>Numerical solution</i>	15
§3 CODE VERIFICATION	17
§3.1 <i>Introduction</i>	17
§3.2 <i>Terminal velocity</i>	18
§3.2.1 <i>Theory</i>	18
§3.2.2 <i>Numerical solutions and simulation code</i>	19
§3.2.3 <i>Results</i>	20
§3.2.4 <i>Conclusion</i>	24
§3.3 <i>Pressure drop over a packed/empty bed</i>	25
§3.3.1 <i>Theory</i>	25
§3.3.2 <i>Numerical solutions and simulation code</i>	25
§3.3.3 <i>Conclusion</i>	26
§3.4 <i>Velocity profile in a rectangular bed</i>	27
§3.4.1 <i>Theory</i>	27
§3.4.2 <i>Results</i>	29
§3.4.3 <i>Conclusion</i>	30
CHAPTER 3: MEASUREMENT TECHNIQUES.....	31
§1 INTRODUCTION	31
§2 PARTICLE IMAGE VELOCIMETRY	31
§2.1 <i>Introduction</i>	31
§2.2 <i>PIV in the experimental setup</i>	33
§3 BUBBLE DETECTION.....	35
§3.1 <i>Introduction</i>	35
§3.2 <i>Bubble detection in the experimental setup</i>	35
§4 PRESSURE PROBE	37
§4.1 <i>Introduction</i>	37
§4.2 <i>Pressure probe in the experimental setup</i>	37
CHAPTER 4: EXPERIMENTAL.....	38
§1 EXPERIMENTAL SETUP	38
§2 EXPERIMENTAL AND SIMULATION RESULTS.....	39
§2.1 <i>Introduction</i>	39
§2.2 <i>Bubble detection</i>	40
§2.2.1 <i>Fluidisation results</i>	40
§2.2.2 <i>Spouting results</i>	43
§2.2.3 <i>Conclusion</i>	44

§2.3 Particle Image Velocimetry.....	45
§2.3.1 Fluidisation results	45
§2.3.2 Spouting results.....	49
§2.3.3 Conclusion	49
§2.4 Pressure measurements.....	50
§2.4.1 Bedheight and pressure fluctuations	50
§2.4.2 Comparing simulation and experiment	51
§2.4.3 Conclusion	52
CHAPTER 5: CONCLUSIONS AND RECOMMENDATIONS.....	53
LITERATURE.....	56
LIST OF SYMBOLS.....	58
APPENDIX A: PRESSURE DROP CALCULATION	59
APPENDIX B: BUBBLE DETECTION RESULTS	60
APPENDIX C: MINIMUM FLUIDISATION	70
APPENDIX D: ENERGY ANALYSIS	71
APPENDIX E: EXPERIMENTAL PROCEDURE.....	72
APPENDIX F: FAST FOURIER TRANSFORM RESULTS.....	73
APPENDIX G: RELATION BETWEEN RMS AND Z-COORDINATE.....	75

Chapter 1: Introduction

§1 Project background

The graduation report lying before you is a part of a larger research project carried out by my supervisor Jeroen Link. The project has a two-fold goal:

1. To obtain a more fundamental understanding of the granulation of fertiliser beads using spout-fluid beds.
2. To enhance this granulation process to obtain a more uniform particle size distribution and to minimise energy consumption.

My assignment was part of the first goal. The computer code that was developed earlier (the discrete particle model, see chapter 2) needed to be verified and validated. Verification encompasses ‘verification’ of the key model equations. These are the gas-solid drag equations and the gas-phase hydrodynamics. More details can be found in chapter 2.

After verification the model needed to be validated, meaning that simulation results were compared with the results from an experimental setup (a pseudo 2D fluidised bed).

To this end, a couple of non-intrusive measurement techniques were employed. These included two visual techniques using a digital camera: bubble detection and particle image velocimetry. The other technique employed a pressure probe, able to obtain data at high frequencies (100 Hz). With the first technique bed voidage and bedheight can be validated while with the second technique particle velocities can be obtained. The third technique is of course able to measure pressure drops. For more details, the reader is referred to chapter 3.

In chapter 4, the experimental procedures and results of both experiment and simulation are presented and interpreted. Some concluding remarks (accompanied with recommendations) about the current code implementation can be found in chapter 5.

However, in order to obtain a thorough understanding of fluidisation phenomena in general and spout phenomena in particular, the reader is first referred to the next paragraph.

§2 Introduction to fluidisation

Gas fluidisation is widely applied in the chemical process industry, because of several advantageous properties like isothermal conditions throughout the bed, excellent heat and mass transfer properties and the possibility of continuous operation [1]. Typical applications cover a wide variety of physical and chemical processes, such as fluidised bed combustion, catalytic cracking of oil, gas-phase polymerisation of olefins and fluidised bed granulation (fertilisers).

§2.1 Regular fluidisation

Fluidised beds differ from fixed beds in the respect that the gas velocity in fluidised beds is increased to such an extent, that the solid particles in the bed are lifted. In other words: in gas-fluidised beds, the gravity force acting on the solid particles is compensated by the drag forces that are exerted on the particles by the upward flowing gas. The term fluidised bed is derived from the observation that particles suspended in the gas show properties similar to boiling liquids and in many ways exhibit liquid-like behaviour [2], as illustrated in figure 1.

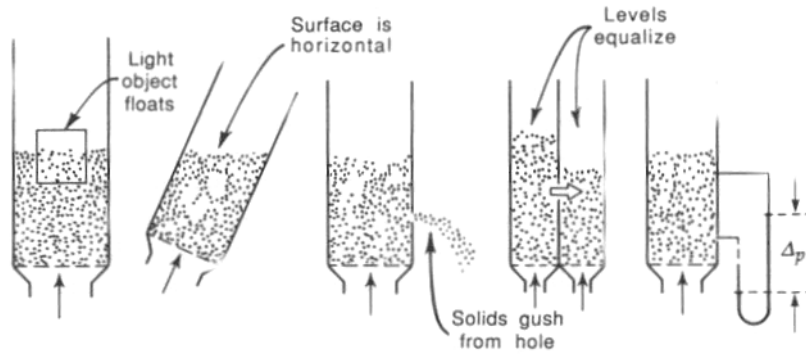


Figure 1: Liquid-like behaviour of fluid bed

The superficial gas velocity at which the gravity and drag forces are just balanced is defined as the minimum fluidisation velocity (u_{mf}). The minimum fluidisation velocity depends on many factors, but the two most important ones are the density and diameter of the particles. With this observation in mind, Geldart [17] developed a particle classification system. In this system, particles are sorted into four groups:

Group A: Aeratable.

Materials having a small mean particle size and/or low particle density ($< \sim 1400 \text{ kg/m}^3$). These solids fluidise easily, with smooth fluidisation at low gas velocities and controlled bubbling with small bubbles at higher gas velocities.

Group B: Sandlike.

Most particles of size $40 \mu\text{m} < d_p < 500 \mu\text{m}$ and density $1400 \text{ kg/m}^3 < \rho_s < 4000 \text{ kg/m}^3$. These solids fluidise well with vigorous bubbling action and bubbles that grow large.

Group C: Cohesive.

Very fine powders. Normal fluidisation is extremely difficult for these solids.

Group D: Spoutable.

Large and/or dense particles. Deep beds of these solids are difficult to fluidise. They behave erratically, giving large exploding bubbles or severe channelling, or spouting behaviour if the gas distribution is very uneven.

At velocities exceeding u_{mf} gas bubbles are usually present in the bed. These bubbles have a profound influence on the hydrodynamics of the bed and therefore on its performance as a heat exchanger or reactor.

Dependent on the gas velocity, there are several different fluidisation regimes. The most important regimes are the bubbling-regime, slug-flow and pneumatic transport [2]. See figure 2 for details.

I: Bubbling-regime (Geldart A+B)

Gas bubbles rise up through the solids in the bed. The diameter of the bubbles is smaller than the diameter of the pipe.

II: Slug-flow (Geldart B+C+D)

The bubbles have almost or completely the same diameter as the pipe. The upward motion of the bubbles has a turbulent effect on the solid particles, which flow downward by the wall around the bubble.

III: Pneumatic transport (All)

In this regime, entrainment of particles occurs and if no means of circulation is provided, the bed will empty.

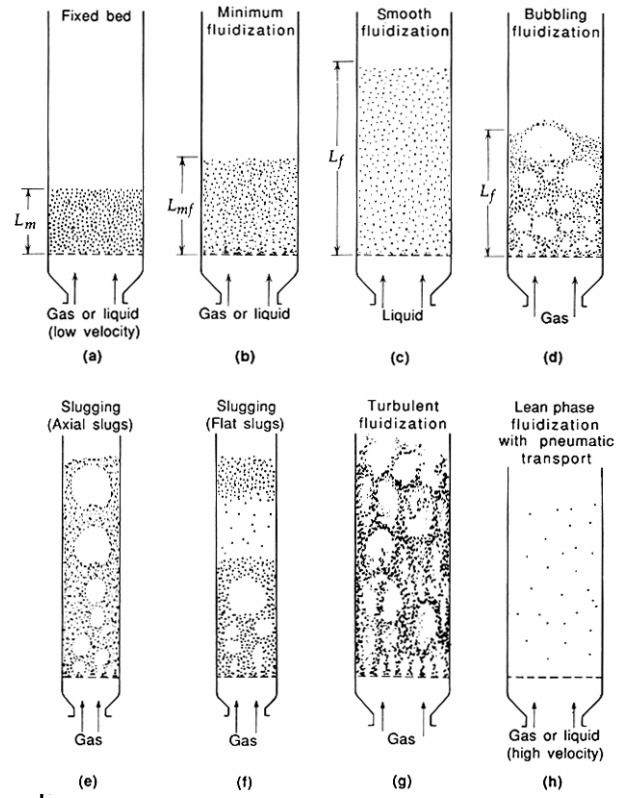


Figure 2: Bed behaviour with increasing gas velocity

§2.2 Spout fluidisation

The fluidised beds shown in figure 2 are based on a uniform gas distribution. Now, the gas flow is increased locally to such an extent that a channel with a low particle hold-up is formed. This type of bed is called the 'spouted' bed. The channel in the bed is called the 'spout' and in this spout there is a fast transport of solids. The solids leave the spout in the fountain area. The region surrounding the spout is called the 'annulus' and in this region there is downward motion of solids. The spouted bed type in all its forms is usually applied to particles of the Geldart D group. An important industrial application for this bed type is the granulation of fertiliser.

Spouted beds can be divided into three categories. The first one is simply called 'spouted bed'. This bed consists of one central nozzle through which the gas is blown. The bed is usually a cylindrical with a conical base. The second one is called 'spout-fluid' bed. This bed also consists of a central nozzle, but has an additional number of smaller nozzles through which fluidisation air is blown. The third one is called 'jet-spouted' bed. Like the 'spouted bed', the bed consists of one central nozzle. However, because of a (much) higher gas flow (and lower solids content) the channel that is typical for spouted beds can no longer be observed.

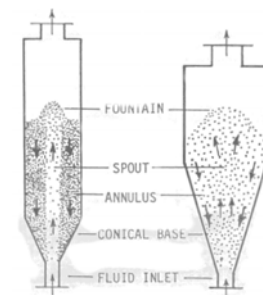


Figure 3: Spouted and jet-spouted bed

The principal of spouting is almost the same for a spouted and a spout-fluid bed. When the gas rate is increased from zero, an internal cavity is formed above the spout nozzle. The internal cavity becomes unstable at increasing spout gas rate and grows to a channel. Finally, a spout channel is formed between the nozzle and the top of the bed [8]. The pressure drop over the bed is relatively high when the spout channel is in the process of being formed, but drops when the spout channel reaches the bed surface. At even higher spout gas rates, an overall circulation of the solid bed material is maintained. Some of the solids in the annulus are flowing into the spout channel at the bottom and are launched into the fountain. Other solids enter the spout higher in the bed. If these solids shortcuts are undesirable, draft tubes –which separate the spout from the annulus- can be installed [11]. In the fountain region, the solids are spread out over the upper surface of the bed. The circulation flow pattern thus consists of an upward flow of solids in the spout channel and a downward flow of solid in the annulus region. With still increasing gas rates, the total bed voidage increases and the jet-spouted regime is reached.

The spouted and spout-fluid beds differ in the process in which a stable spouting regime is obtained. As can be seen in figure 4, increasing gas flow in the spouted bed increases the length of the spout channel until the bed surface is reached. The spout-fluid bed however goes through several different regimes before a stable spouting regime is obtained.

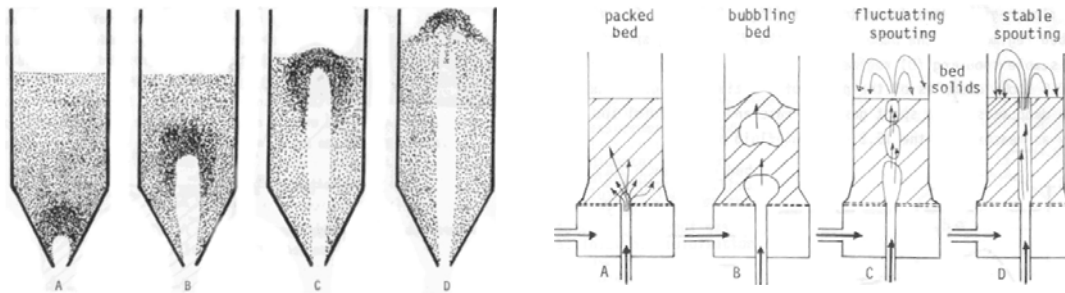


Figure 4: left-hand side being a spouted bed, right-hand side being a fluid-spout bed

One of the advantages of spout-fluid beds over spouted beds is a higher recirculation rate of the solids. Also, the auxiliary air increases the fluid-solid contact in the annulus and reduces the likelihood of particle agglomeration, dead zones and sticking to the wall of the vessel [12].

An advantage of the spout-fluid bed over a fluidised bed is the possibility of operating in a wider range of gas flow rates without coming to slug-flow, which generally reduces the efficiency of the system [12]. Also, the bed gives no separation with mixed particles of different diameters and densities [9].

Chapter 2: The Model

§1 The Discrete Particle Model

§1.1 Introduction

The model used in this work is a so-called ‘Discrete Particle Model’, DPM for short. In this chapter, the theory of the discrete particle model will be presented. The first paragraph treats the multi-scale concept and the position that the discrete particle model takes within this concept. In the second paragraph, the most important equations for the collision model and gas-phase hydrodynamics will be discussed.

§1.2 Multi-scale concept

For gas-fluidised beds, three different scales of fundamental models can be distinguished. These models are part of a multi-scale concept for fundamental hydrodynamic models of gas-fluidised beds (see figure 1).

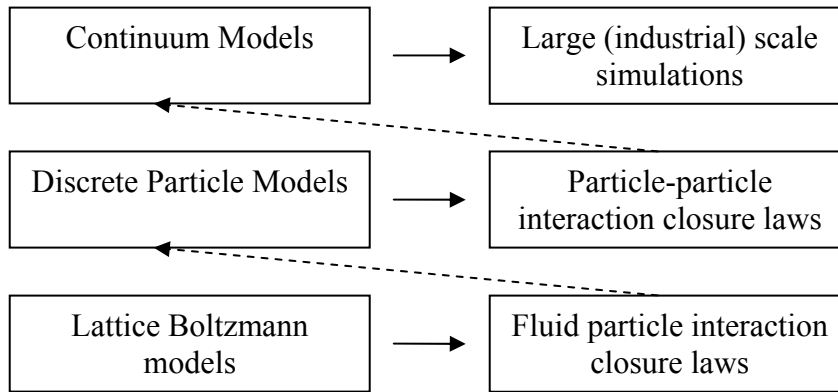


Figure 1: Multi-scale concept

1. In order to model a large (industrial) scale fluidised bed, a continuum model (where the gas-phase and the solids phase are regarded as interpenetrating continuous media) is the appropriate choice. This Eulerian-Eulerian type of model has been developed and successfully applied over the last two decades (Kuipers *et al.* 1992, Gidaspow, 1994 among many others). These models require closure relations for the solids phase stress tensor and the fluid-particle drag. In the absence of more accurate closures [1] common empirical relations are used.

2. In discrete particle models the Newtonian equations of motion are solved for each individual solid particle in the system. Compared to continuum models, this Eulerian-Lagrangian type of model no longer requires a closure relation for the solids phase rheology since the motion of the individual particles is solved directly. However, the number of particles that can be taken into account in this technique is limited ($< 10^6$). Therefore, it is not yet possible, even with modern super computers, to simulate a large (industrial) scale system ($> 10^9$). On the other hand, this type of model can be used to arrive at improved closure equations for continuum models by employing techniques from statistical mechanics. Since the discrete particle models are very well suited to study the influence of particle properties on the hydrodynamics of gas-fluidised beds, this

makes them very useful models within the multi-scale modelling concept. However, discrete particle models still require closure relations for the fluid-particle drag, since the gas flow is resolved on a length scale larger than the particle size. In the absence of better closures, empirical relations for the fluid-particle drag have to be used [1].

3. When the gas flow is resolved on a length scale smaller than the particle size, these empirical closure relations for fluid-particle drag are no longer required. Instead, they can actually be obtained from the simulations. The Lattice Boltzmann technique seems to be best suited for such simulations because it is very flexible in dealing with complex flow geometries. It is important to know that such simulations are limited to systems consisting of a number of particles that is significantly smaller ($<10^3$) than the number of particles that can be taken into account using discrete particle models ($<10^6$).

In short, the multi-scale concept, as presented in figure 1, consists of three classes of models. Going from continuum models via discrete particle models to Lattice Boltzmann models, more detail of the two-phase flow is resolved. This is accompanied by increased computation requirements which necessitate a size reduction of the simulated system. The model capable of simulating a larger system is fed with closure relations obtained from a more detailed model. Before a connection between separate scales can be established, the individual simulation techniques must be well developed, verified and experimentally validated.

§1.3 Discrete Particle Modelling

Two very important parts of the discrete particle model are the manner in which particles interact with each other and with the gas phase. In the first section, the collision model used in the simulation code will be presented. In the second section, equations necessary for solving the gas-phase hydrodynamics will be discussed. In the last section, coupling between particle motion and gas-phase hydrodynamics will be presented.

§1.3.1 Particle-particle interaction

Different approaches can be used for describing particle-particle interactions during collision. Two important ones are the soft-sphere and the hard-sphere approaches. In the hard-sphere model, transport of impulse is achieved via Newton's second and third law. In the soft-sphere model, transport of impulse is achieved via a linear spring/dash-pot model. Hard-sphere simulations can be typified as 'event driven'. In event driven models, the progression depends on the number of collisions that occur. Such models are often used in situations when the interaction times are small compared to free flight times. Soft-sphere models can be typified as 'time driven'. In time driven models, a constant time step is used to progress through the dynamics of the system. Such models are often used in situations when the interaction times are large compared to free flight times.

For dynamic systems, a hard-sphere model is generally computationally faster than a soft-sphere model as long as there is sufficient motion in the system and the void fraction does not become too low. Severe problems are encountered when static situations like for example defluidisation occur. The particles become very closely packed with very low relative velocities. The number of collisions then increases exponentially whilst the impulse exchange concerned with a single collision becomes negligible.

A soft-sphere model has no problems in dealing with static situations and is therefore to be preferred for simulations where such situations occur.

In the code used in this work, only the hard-sphere approach is used. This is because the code will be used primarily for simulations at high gas velocities (e.g. spout-fluid bed). For more details about the soft-sphere approach, the reader is referred to the Ph.D. thesis of B.P.B. Hoomans (2000).

In the hard-sphere model, the particles are assumed to interact through binary, quasi-instantaneous collisions where contact occurs at a point. The particles are perfect, homogeneous spheres and the interaction forces are impulsive. In between collisions, the particles are in free flight.

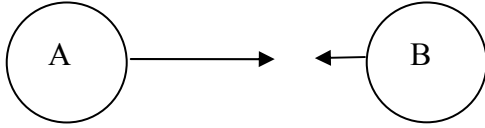


Figure 2: Particle collision

For a binary collision of these particles, the following equations can be derived by applying Newton's second ($F=m.a$) and third laws (action= - reaction). It must be mentioned that all the bold characters in these equations represent vectors.

From (1) and (2)

$$m_a (\mathbf{v}_a - \mathbf{v}_{a,0}) = \mathbf{J} \quad (1)$$

$$m_b (\mathbf{v}_b - \mathbf{v}_{b,0}) = -\mathbf{J} \quad (2)$$

and (3) and (4)

$$I_a (\omega_a - \omega_{a,0}) = -(R_a \mathbf{n}) \times \mathbf{J} \quad (3)$$

$$I_b (\omega_b - \omega_{b,0}) = R_b \mathbf{n} \times (-\mathbf{J}) \quad (4)$$

follow (5) and (6)

$$m_a (\mathbf{v}_a - \mathbf{v}_{a,0}) = -m_b (\mathbf{v}_b - \mathbf{v}_{b,0}) = \mathbf{J} \quad (5)$$

$$\frac{I_a}{R_a} (\omega_a - \omega_{a,0}) = \frac{I_b}{R_b} (\omega_b - \omega_{b,0}) = -\mathbf{n} \times \mathbf{J} \quad (6)$$

With:

$$\mathbf{n} = \frac{\mathbf{r}_a - \mathbf{r}_b}{|\mathbf{r}_a - \mathbf{r}_b|} \quad (7)$$

$$I = \frac{2}{5} m R^2 \quad (8)$$

The impulse vector is defined as follows:

$$\mathbf{J} = \int_{t=0}^{t=t_c} \mathbf{F}_{ab} dt \quad (9)$$

where t_c stands for the contact time (*i.e.* the duration of the contact).

From equations (5) and (6) it is clear that the post-collision velocities of both particles can be calculated when the impulse vector \mathbf{J} is known. In simulations of gas-fluidised beds, a large number of collisions have to be processed and therefore the actual physics of a binary collision has to be simplified to some extent and constitutive relations have to be introduced in order to calculate the impulse vector \mathbf{J} . Through these constitutive relations, three parameters enter the model. The first parameter is the coefficient of (normal) restitution e , ($0 \leq e \leq 1$). Second parameter is the coefficient of (dynamic) friction μ , ($\mu \geq 0$). The third parameter is the coefficient of tangential restitution β , ($0 \leq \beta_0 \leq 1$). Although it is accepted that these coefficients depend on particle size and impact velocity, this is not taken into account in this model. These three parameters are very important because they determine the nature of the collisions. The values of the three parameters were measured earlier and put into the model.

For a more detailed mathematical deduction and more information about the three parameters, the reader is referred to the Ph.D. thesis of B.P.B. Hoomans (2000) .

§1.3.2 Gas-particle interaction

Collisions are not the only forces that act on a particle in a fluid bed. Other forces include gravity, drag and pressure gradients. All of these ‘external’ forces are accounted for in the following equation:

$$m_p \frac{d\mathbf{v}_p}{dt} = m_p \mathbf{g} + \frac{V_p \beta}{(1 - \varepsilon)} (\mathbf{u} - \mathbf{v}_p) - V_p \nabla p \quad (10)$$

where m_p represents the mass of a particle, \mathbf{v}_p its velocity, \mathbf{u} the local gas velocity and V_p the volume of a particle. The first term of the right-hand side of equation (10) represents gravity, the second term the drag force caused by the gas-phase and the last term represents the effects of pressure gradients. β represents an inter-phase momentum exchange coefficient.

The correlations used to describe this coefficient depend on the void fraction. For low void fractions ($\varepsilon < 0.80$), β is obtained from the Ergun equation:

$$\beta = 150 \frac{(1 - \varepsilon)^2}{\varepsilon} \frac{\mu_g}{D_p^2} + 1.75(1 - \varepsilon) \frac{\rho_g}{D_p} |\mathbf{u} - \mathbf{v}_p| \quad (11)$$

For high void fractions ($\varepsilon \geq 0.80$) the following expression presented by Wen and Yu (1966) is used:

$$\beta = \frac{3}{4} C_d \frac{\varepsilon(1 - \varepsilon)}{D_p} \rho_g |\mathbf{u} - \mathbf{v}_p| \varepsilon^{-2.65} \quad (12)$$

The drag coefficient (C_d) is a function of the particle Reynolds number:

$$C_d = \begin{cases} \frac{24}{\text{Re}_p} (1 + 0.15 \text{Re}_p^{0.687}) & \text{Re}_p < 1000 \\ 0.438 & \text{Re}_p \geq 1000 \end{cases} \quad (13)$$

The particle Reynolds number in this case is defined as:

$$\text{Re}_p = \frac{\varepsilon \rho_g |\mathbf{u} - \mathbf{v}_p| D_p}{\mu_g} \quad (14)$$

Since the particle and fluid interactions are intertwined, they need to be coupled in order to simulate a fluid-bed correctly. This coupling is accomplished through the source term \mathbf{S}_p (equation 19). The voidage which is necessary for the continuity and momentum equations of the gas-phase is calculated from the particles' positions in the grid, which – on its turn- depends on the results of the collision model.

§1.3.3 Gas-phase Hydrodynamics

The calculation of the gas-phase hydrodynamics is based on the numerical solution of the Navier-Stokes equations, which are augmented with a particle-gas interaction term.

Continuity equation gas phase:

$$\frac{\partial(\varepsilon \rho_g)}{\partial t} + (\nabla \cdot \varepsilon \rho_g \mathbf{u}) = 0 \quad (15)$$

Momentum equation gas phase:

$$\frac{\partial(\varepsilon \rho_g \mathbf{u})}{\partial t} + (\nabla \cdot \varepsilon \rho_g \mathbf{u} \mathbf{u}) = -\varepsilon \nabla p - \mathbf{S}_p - (\nabla \cdot \varepsilon \boldsymbol{\tau}_g) + \varepsilon \rho_g \mathbf{g} \quad (16)$$

The two basic variables in the model are the pressure (p) and the velocity of the gas-phase (u_x , u_y and u_z). The void fraction (ε) and the momentum exchange source term (\mathbf{S}_p) are obtained earlier.

The gas phase density (ρ_g) is related to the pressure and the gas phase temperature (T) by the ideal gas law:

$$\rho_g = \frac{M_g}{RT} P \quad (17)$$

The viscous stress tensor ($\boldsymbol{\tau}_g$) is assumed to depend only on the gas motion. The general form for a Newtonian fluid (*Bird et al.*, 1960) is used:

$$\boldsymbol{\tau}_g = - \left[\left(\lambda_g - \frac{2}{3} \mu_g \right) (\nabla \cdot \mathbf{u}) \mathbf{I} + \mu_g \left((\nabla \mathbf{u}) + (\nabla \mathbf{u})^T \right) \right] \quad (18)$$

In the simulations, the bulk viscosity of the gas phase (λ_g) was set equal to zero which is allowed for gases (Bird *et al.*, 1960) whereas for the gas phase shear viscosity a constant value of $\mu_g = 1.8 \cdot 10^{-5}$ kg/m.s was used. \mathbf{I} denotes the unit tensor.

The reaction force to the drag force exerted on a particle per unit volume is included in the momentum equation (16) via a source term \mathbf{S}_p :

$$\mathbf{S}_p = - \frac{1}{V} \int \sum_{a=0}^{N_{part}} \frac{V_p \beta}{(1 - \varepsilon)} (\mathbf{u} - \mathbf{v}_a) \delta(\mathbf{r} - \mathbf{r}_a) dV \quad (19)$$

§2 Numerical implementation

§2.1 Division of bed in computational cells

The simulation code incorporates the (discretised) equations for particle motion and for the gas-phase hydrodynamics.

The code in its current form solves the particle motion and gas-phase hydrodynamics in three dimensions. For a schematic view of the coordinate system, see figure 3.

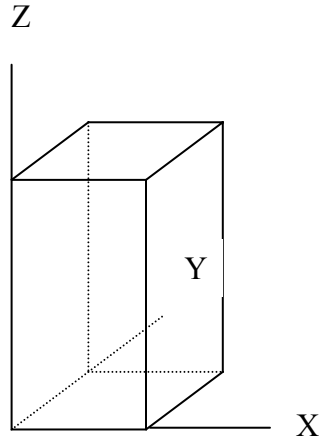


Figure 3: Coordinate system of DPM

To numerically solve a fluidisation process that is taking place inside this box, the box has to be divided into smaller cells (a grid). The size of these computational cells has to be carefully selected to keep computational time to a minimum and to guarantee correct simulation results. An important incentive for transmuting the code to three dimensional hydrodynamics is covered in the next section.

A major disadvantage of solving the gas-phase in two dimensions was the limitation in the number of computational cells in the y-direction. The code allows for only one cell to

be set up. The x- and z-direction can contain as many cells as are needed. Consequence of the one-cell limit in the y-direction is a limited choice in bed depth. This means that with the current code, only quasi two-dimensional beds can be simulated. For the work done on the two-dimensional experimental setup (x-, y-, z-dimensions are 15 cm, 1.5 cm and 100 cm), this is of no great importance since there will be a negligible gas-phase velocity profile in the y-direction. For the simulation of this bed, cells of 1x1.5x1 cm were specified.

For the three-dimensional experimental setup that is to be used in the future (x-, y-, z-dimensions are 15.4, 8.4 and 140 cm), it is expected that the code does not suffice. Therefore the implementation of the gas-phase hydrodynamics was extended to the full three dimensions.

This enhancement of the code was crucial in order to simulate a spout-fluid bed in a three-dimensional bed. See figure 4. Without a proper three-dimensional code, the complete depth of the bed will be specified at spout velocity. As becomes clear from the picture on the right-hand side, implementation of the three-dimensional code removes his problem.

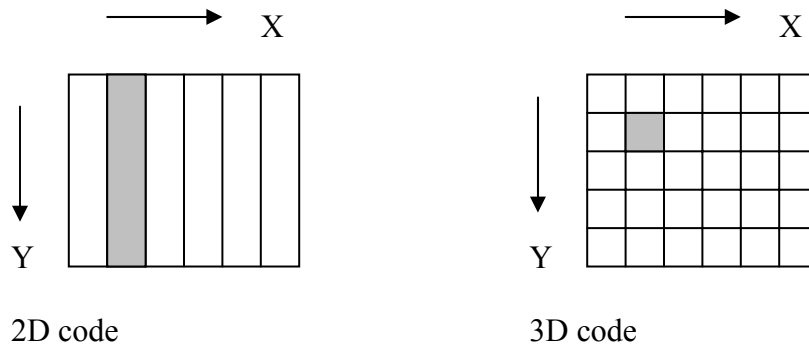


Figure 4: Bottom of a simulated column

§2.2 Numerical solution

The numerical solution of the gas-phase hydrodynamics (equations 15 and 16) is obtained by the use of a finite difference technique employing a staggered grid to ensure numerical stability. This implies that the scalar variables (e.g. P and ε) are defined at the cell centre and that the velocity components are defined at the cell faces as shown in figure 5.

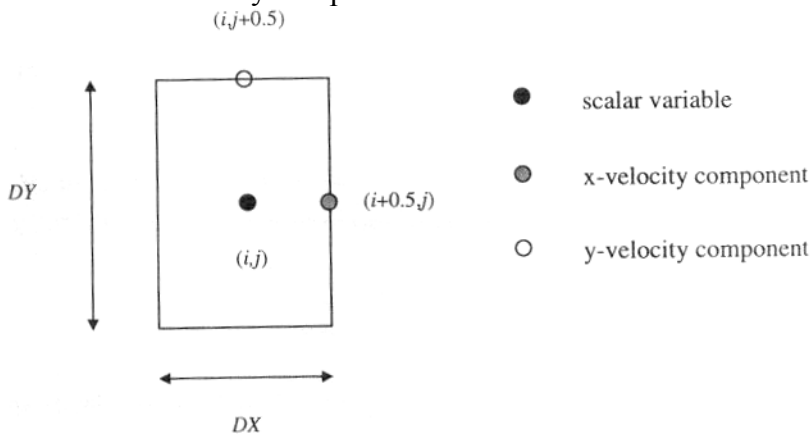


Figure 5: Staggered grid

The following simplified scheme shows the different stages during the simulation of a fluid bed.

1. Initialisation

The input files containing pressures and gas-phase velocities and particle positions, radii, rotational and translational velocities are read. In addition to this, an input file containing parameter settings and constants is read. Using this input, derived variables like particle mass are calculated.

After this initialisation, the main loop of the code is entered. As long as the actual time does not exceed the user-specified stop time and no errors occur, the simulation continues with a certain time-step.

2. Interaction gas-particle

Within the loop, first the particle velocities are updated by calculating the forces acting on a particle. This requires the interpolation of the variables concerning the flow field (known in the staggered grid) to the grid in which the particles move (Lagrangian grid). After this, the inter-phase momentum exchange coefficient (β) can be calculated for each particle using the Ergun (11) and the Wen and Yu equations (12). After this, the source term (\mathbf{S}_p) can be calculated.

3. Processing of the collisions

A sequence of collisions is processed, one collision at a time, using the hard-sphere collision model. The collisions continue until a user-specified time step (DT) is exceeded. After this time step, the new positions and velocities of the particles are known.

4. Interaction particle-gas

In order to solve the flow field at this new time level, the particle positions known in the Lagrangian grid have to be converted to the staggered grid. Now, the voidage (ε) can be calculated.

5. Gas-phase flow solver

The flow field can be solved using the Navier-Stokes equations and the continuity equation. To this end, a solver is used. Now, the new gas velocity and pressure are known.

6. Data saving

The data is written to specified output files.

A schematic overview of the computational flowchart can be found in figure 6.

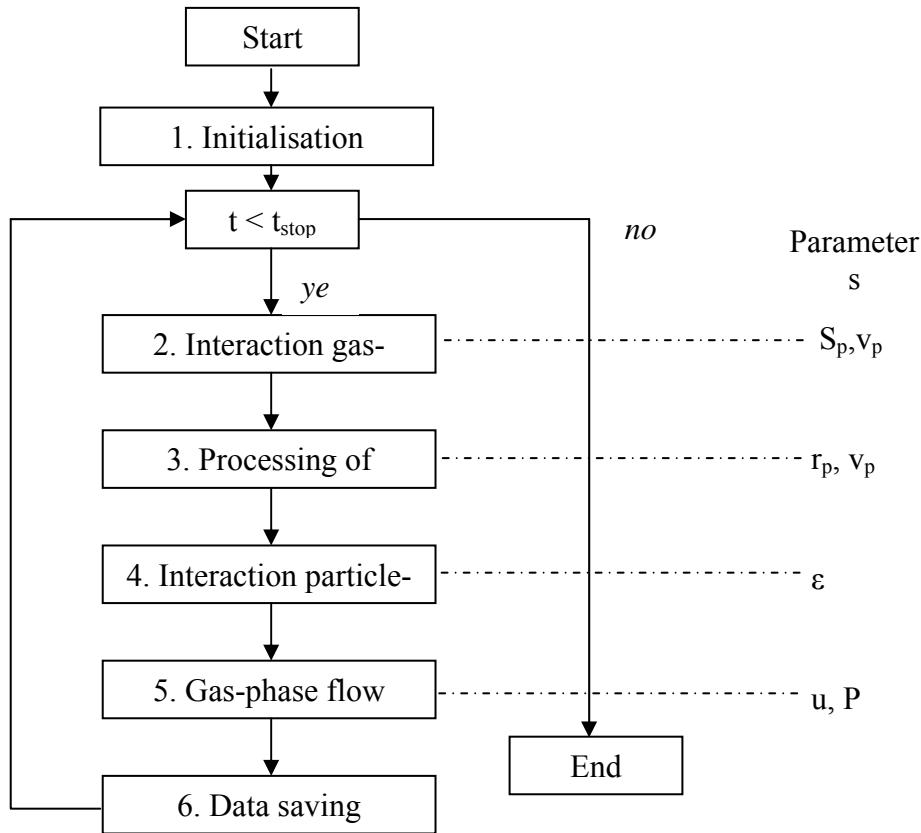


Figure 6: Computational flowchart

§3 Code verification

§3.1 Introduction

Before results from simulations can be compared to data obtained from experimental set-ups (validation), the simulation code needs to be verified. Equations programmed into the code should also ‘come out’.

A key part of the discrete particle model is the interaction between gas and particles. The terminal velocity provides information about the drag relation for high bed voidage ($\epsilon > 0.8$): the Wen&Yu equation. The packed bed arrangement provides information about the drag relations for low bed voidage ($\epsilon < 0.8$): the Ergun equation.

Another important part of the model is the flowsolver which calculates the gas velocity for all the grid cells in the bed using the Navier-Stokes equations. The implementation of these equations can be verified by comparing the velocity profiles of the code with velocity profiles obtained by solving these equations analytically (using some assumptions).

§3.2 Terminal velocity

§3.2.1 Theory

The terminal velocity of a falling particle is a result of all the forces acting on such a particle. These forces are the gravity force (F_g), the buoyant force (F_u) and the friction force between the fluid (gas) and the particle (F_f). In this case, the direction of the gravity force is pointed downward, buoyant force and friction are pointed upward.

$$m_p \frac{dv_p}{dt} = \sum F = F_f + F_u - F_g \quad (20)$$

One finds:

$$\frac{1}{6} \pi d_p^3 \rho_p \frac{dv_p}{dt} = C_w \frac{1}{4} \pi d_p^2 \frac{1}{2} \rho_f v_p^2 + \frac{1}{6} \pi d_p^3 (\rho_f - \rho_p) g \quad (21)$$

or

$$\frac{dv_p}{dt} = C_w \frac{3}{4} \frac{1}{d_p} \frac{\rho_f}{\rho_p} v_p^2 + \frac{\rho_f - \rho_p}{\rho_p} g \quad (22)$$

In this equation, C_w is a dimensionless friction coefficient which depends on the particle Reynolds number. It has the same function as the drag coefficient (C_d) in being the interaction parameter between gas-phase and particle (see §1.3.2). In order to obtain a more cohesive report, the term “drag coefficient” will be used from this point on but will retain the symbol C_w in the equations.

The correlations for the drag coefficient depend on the particle Reynolds number.

$$\text{Re}_p = \frac{\varepsilon \rho_f u_f d_p}{\eta} \quad (23)$$

Three regions can be distinguished:

Stokes	$\text{Re}_p < 0.1$	$C_w = \frac{24}{\text{Re}_p}$	
Intermediate	$\text{Re}_p < 1000$	$C_w = \frac{24}{\text{Re}_p} (1 + 0.15 \text{Re}_p^{0.687})$	(24)
Newton	$\text{Re}_p \geq 1000$	$C_w = 0.438$	

The correlation for the intermediate region can also be used for $Re < 0.1$ and is therefore more widely applied than the equation specifically for the Stokes region. In the code, the equations for the intermediate and Newton regions are implemented.

When calculating the terminal velocity of a falling particle, the left-hand side of equation (22) goes to zero. For the Stokes region, inserting the relation for C_w reduces it to:

$$v_{p,\infty} = \frac{(\rho_f - \rho_p)gd_p^2}{18\mu_g} \quad (25)$$

with $v_{p,\infty}$ the terminal velocity.

For the intermediate and the Newton regions, it reduces to:

$$v_{p,\infty} = -\sqrt{\frac{4 d_p (\rho_p - \rho_f)g}{3 C_w \rho_f}} \quad (26)$$

Since C_w in equation (26) is a function of v_p , this equation has to be solved iterative.

The implementation of the drag coefficients in the simulation code for the area of interest is the one proposed by Wen & Yu. However –as previously mentioned- Wen & Yu only have equations for the intermediate and Newton regions. Therefore, one can expect the terminal velocity from the simulation code to deviate somewhat from Stokes' equation. The maximum deviation would amount to 3 % (being $0.15 \cdot 0.10^{0.687}$). For a small number of simulations, the Stokes equation was temporarily added to the code to verify if the code would indeed give a more accurate result.

§3.2.2 Numerical solutions and simulation code

For all three regions, equation (22) was solved using the spreadsheet program Excel. Using time steps of the same size as in a simulation (10^{-4} seconds), the following set of equations is solved:

$$a_t = C_w \frac{3}{4} \frac{1}{d_p} \frac{\rho_f}{\rho_p} v_t^2 + \frac{\rho_f - \rho_p}{\rho_p} g \quad (27)$$

$$v_{t+\Delta t} = a_t \Delta t + v_t \quad (28)$$

Equation (22) can easily be solved analytically for the Stokes region. Integration results in:

$$v_t = \frac{(\rho_f - \rho_p)d_p^2 g}{18\mu_g} \left(1 - e^{-\frac{18\mu_g t}{d_p^2 \rho_p}} \right) \quad (29)$$

This equation will be used to verify if the numerical integration of Stokes in Excel gives an accurate enough result. Since this was the case (deviation about 0.001 %), numerical integration in Excel can be used to compare the intermediate and Newton results from simulations.

To obtain the appropriate Reynolds conditions for the three different regions in the simulations, the particle diameter was varied. For simulations in the Newton, intermediate and Stokes regions, particle diameters of 2.5 mm, 0.25 mm and 0.025 mm were used, respectively. Values for other important variables can be found in table 1.

ρ_p	2525	[kg/m ³]
ρ_f	1.198	[kg/m ³]
μ_g	1.8.10 ⁻⁵	[kg/m.s]
g	9.81	[m/s ²]

Table 1: Important variables

The particle, with no initial translational or rotational velocities, was fixed in the top section of an empty column. The gas phase velocity was set to 0 m/s and the particle was released when the simulation begins.

In addition to verifying the particle velocity, some effects of the number of computational cells and wall properties were investigated. Further on, one simulation in the intermediate region with an alternate gravity constant was performed. A gravitational constant of 5 m/s² was used. The theoretical terminal velocity for this situation is 1.1414 m/s and this value was indeed obtained in the simulation.

§3.2.3 Results

According to the input equations, the terminal velocity for the three regions should theoretically be:

	D_p (mm)	$v_{p,\infty}$ (m/s)	Re ($\epsilon=1$)
Newton	2.5	12.5415	2087
Intermediate (g=9.81)	0.25	1.85103	30.80
Intermediate (g=5.00)	0.25	1.14105	19.0
Stokes	0.025	0.047759	0.080

Table 2: Terminal velocities

It must be noted that the Reynolds numbers in table 2 are calculated using a voidage fixed on 1.0. This voidage was chosen because of the manner in which the local cell voidage is calculated. The voidage is calculated applying a volume averaging technique which uses the voidages of neighbouring cells. In case of a column with NZ=1, the bottom voidage (always set to 0.4) would have a too profound effect.

While simulating a column with a height of 1.5 km, it was discovered that the terminal velocity was reached within the first 150 m. For the verification of the Newton region, simulations using the key properties as shown in table 3 were carried out.

<i>Newton</i>	X_{\max}	Y_{\max}	Z_{\max}	NX	NY	NZ	Slip condition	Velocity (m/s)	Relative mean deviation
---------------	------------	------------	------------	----	----	----	----------------	----------------	-------------------------

1	0.15	0.15	150	5	5	1	Free Slip	12.5445	0.095 %
2	0.15	0.15	150	5	5	1	No Slip	12.5445	0.095 %
3	0.03	0.03	150	1	1	1	Free Slip	12.5445	0.095 %
4	0.03	0.03	150	1	1	1	No Slip	12.5445	0.095 %
5	0.03	0.03	150	5	5	120	Free Slip	Oscillates	N.A.

Table 3: Newton simulations

In this table X_{\max} , Y_{\max} and Z_{\max} are the dimensions of the column in each direction. NX , NY and NZ are the number of computational cells in each direction.

In order to take into account the deviation between simulation and Excel results, the deviation between the velocities was calculated for every time-step (10^{-4} sec). After this, the deviations were added and divided by the total number of time-steps to deliver a mean deviation per time step. The mean deviation is divided by the appropriate terminal velocity to acquire a relative mean deviation.

It must be mentioned that only data for the first 5.5 seconds (55001 data points) were used for the calculation of the deviation. The eventual terminal velocity deviates only 0.024 % from the theoretical value, but due to spreadsheet limitations this point in time was not included.

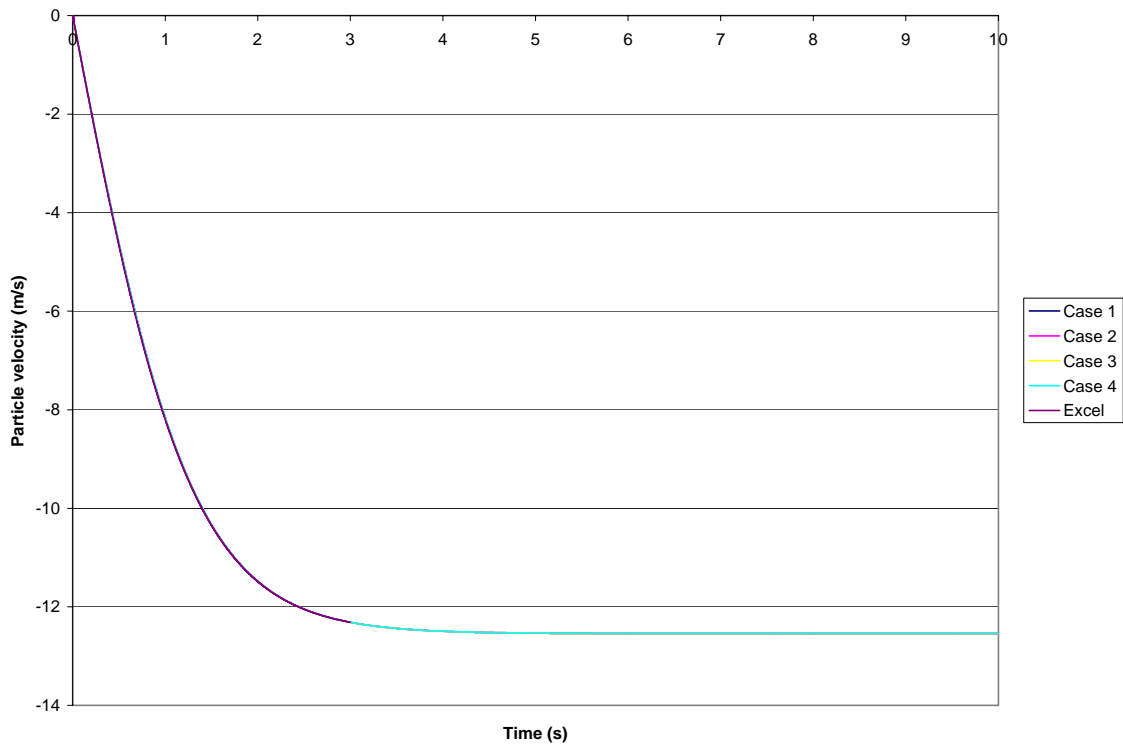


Figure 7: Newton regime

A glance at the deviations in table 3 shows that slip condition and number of cells in x- and y-direction does not have a significant effect on the terminal velocity. This was to be expected since a bed of only one cell high was used. In this way, no pressure gradients (and thus gas velocity and gas densities, which influences drag) could develop in the z-direction.

The deviation of only 0.095 percent during the first 5.5 seconds and the deviation of only 0.024 % in eventual terminal velocity indicates a correct implementation of the drag equations.

Increasing the number of cells in the z-direction beyond 1 showed that terminal velocity was reached after approximately 2.3 seconds. The velocity however did not stabilise, but started oscillating around the terminal velocity. Amplitude of the oscillation however decreased steadily within the simulated 10 seconds.

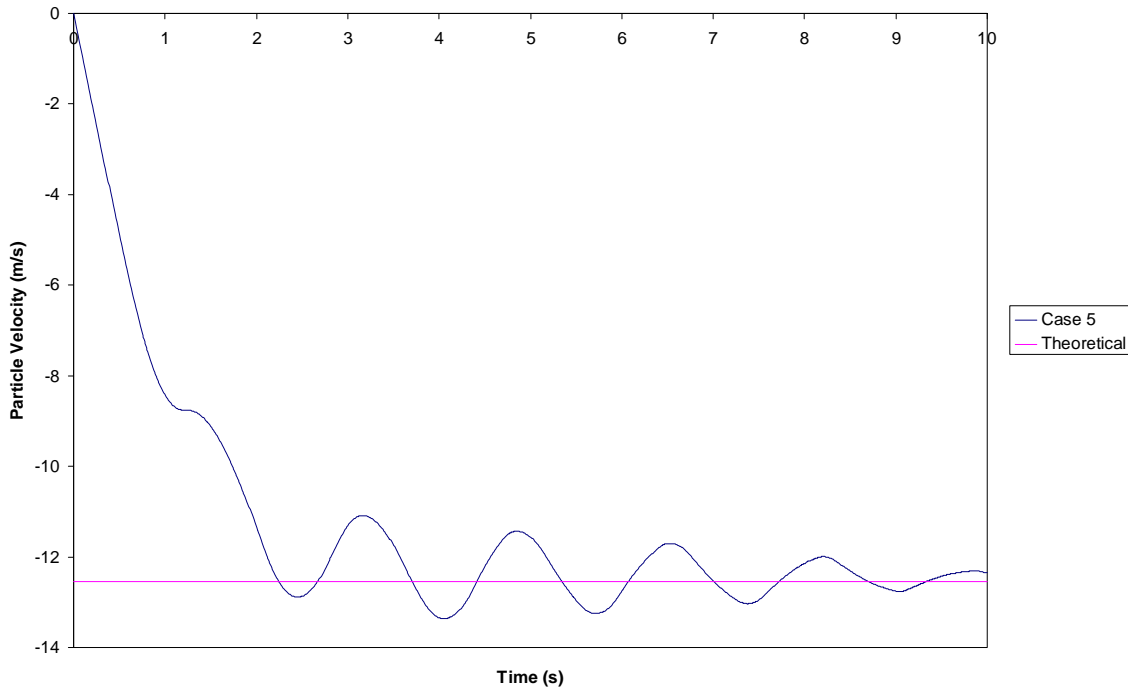


Figure 8: Newton Case 5

Studying the gas velocities in the z-direction, it was discovered that this velocity increased profoundly during the particles fall (values of more than 1 m/s were found). At one time, the gas velocity was directed downward, effectively increasing the particle velocity beyond the terminal velocity. Another time, the gas velocity was directed upward, decreasing the particle velocity.

Since the drag-relations were shown earlier to be correctly implemented, it expected that the flowsolver causes the problem. This problem is not the case in the rest of the simulations since these columns consisted of only one cell so that no gas-phase velocity could develop (one could also obtain this result by shutting down the flowsolver).

Verifying the intermediate region, simulations using the key properties as shown in table 4 were carried out.

<i>Intermediate</i>	X_{\max}	Y_{\max}	Z_{\max}	NX	NY	NZ	Slip condition	Velocity (m/s)	Relative mean dev.
1	0.03	0.03	50	1	1	1	Free Slip	1.851649	0.035 %
2 (g=5 m/s²)	0.03	0.03	50	1	1	1	Free Slip	1.141444	0.035 %

Table 4: Intermediate simulations

The eventual terminal velocity of Case 1 deviates only 0.033 % from the theoretical value. The eventual terminal velocity of Case 2 deviates only 0.035 % from the theoretical value.

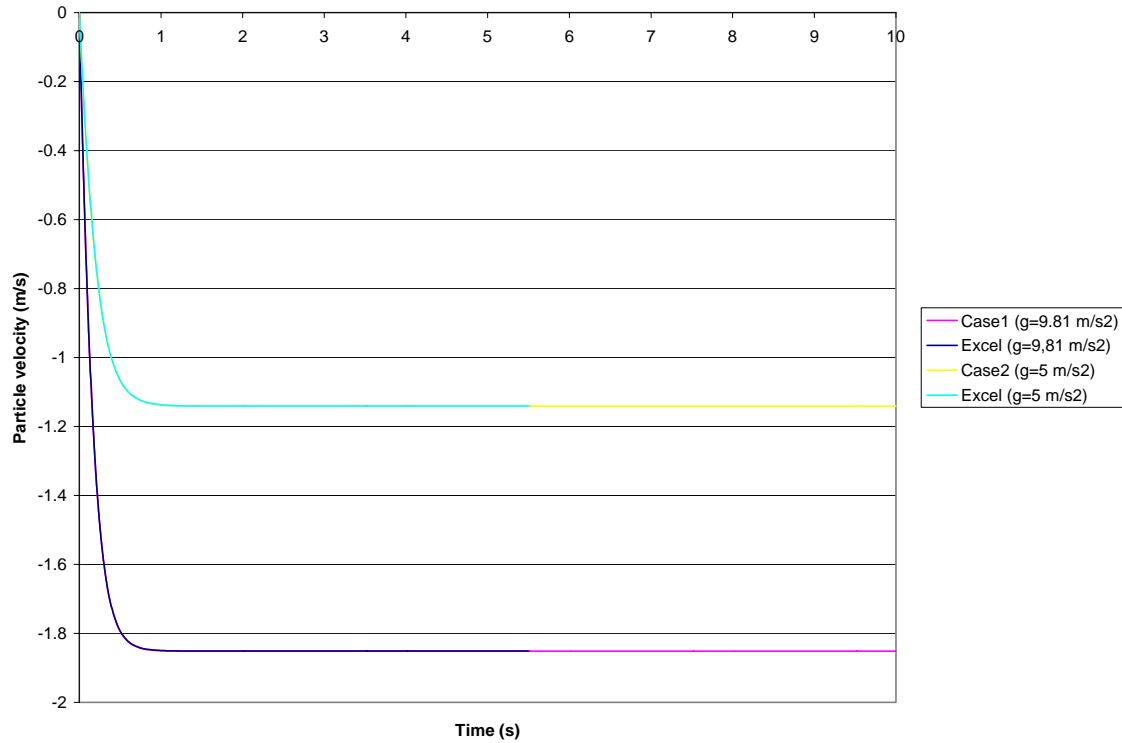


Figure 9: Intermediate Regime

Verifying the Stokes region, simulations using the key properties as shown in table 5 were carried out.

<i>Stokes</i>	X_{\max}	Y_{\max}	Z_{\max}	NX	NY	NZ	Slip condition	Velocity (m/s)	Relative mean dev
1 (Wen&Yu)	0.03	0.03	10	1	1	1	Free Slip	0.046577	2.47 %
2 (Stokes)	0.03	0.03	10	1	1	1	Free Slip	0.047782	0.049 %

Table 5: Stokes simulations

As can be seen in table 5, the implementation of Wen&Yu causes a large deviation (2.47 %) from the terminal velocity. The correct velocity is not reached. As was to be expected, replacing Wen&Yu with the Stokes equation in the simulation code improves the situation dramatically. Case 2 has only a deviation of 0.049 %. The eventual terminal velocity deviates only 0.048 %.

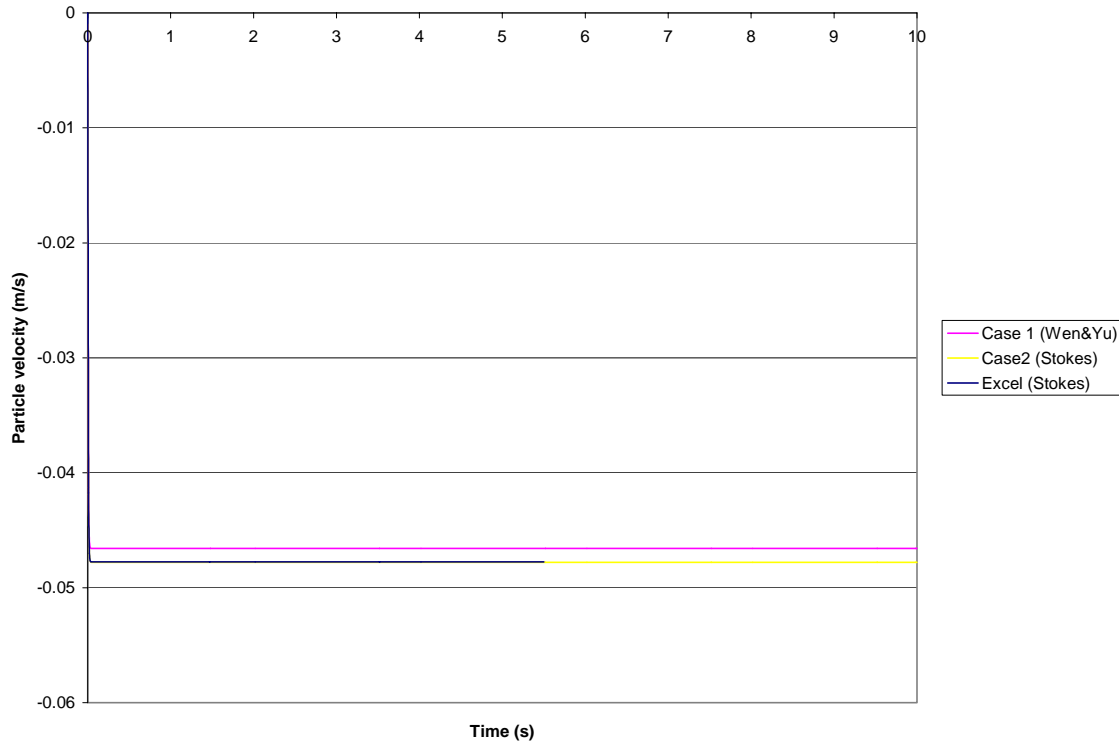


Figure 10: Stokes Regime

§3.2.4 Conclusion

Based on the only the small deviations, it can be concluded that the Newton and intermediate regions were correctly implemented in the simulation code. The Stokes region shows a maximum deviation of about 3 percent, caused by the implementation of Wen&Yu. Implementation of the Stokes equation in the code produced –naturally- the best results, with deviations of about 0.049 percent.

A simulation in the intermediate region with a different gravitational constant also delivered the correct terminal velocity. As was to be expected, variation of boundary conditions does not have a significant influence on the deviations when using a bed with a height of only one cell.

A simulation using multiple cells in the z-direction showed an oscillating behaviour of the particle velocity. Since the drag relations were shown to be correctly implemented, it is expected that the flowsolver is the cause of this problem. Further investigation is recommended.

§3.3 Pressure drop over a packed/empty bed

§3.3.1 Theory

The pressure drop over a packed bed can be calculated using the well-known Ergun equation:

$$\frac{\Delta P}{L} = 150 \frac{(1-\varepsilon)^2}{\varepsilon^3} \frac{\mu_g v_0}{d_p^2} + 1.75 \frac{(1-\varepsilon)}{\varepsilon^3} \frac{\rho_g v_0^2}{d_p} \quad (30)$$

The equation is introduced in the model through the relation for the drag between gas-phase and particle. Note must be taken that this equation is only used for local bed voidages smaller than 0.8. For voidage higher than 0.8, the drag relation of Wen&Yu is used (see paragraph 1.3.2).

§3.3.2 Numerical solutions and simulation code

To be able to measure the pressure drop of a fixed bed in the discrete particle model, one must adjust certain parameters in the code. First are –naturally- the velocities in x-, y- and z-direction of all the particles. These should be set to zero. Further on, the gravity should be set to zero, to avoid the pressure drop caused by the mass of the gas.

For an accurate calculation of the pressure drop, one has to know the precise values of the bed voidage (ε), dynamic gas viscosity (μ_g), superficial gas velocity (v_0), gas density (ρ_g) and particle diameter (d_p). However, most of these numbers depend on the local pressure, which depends on the position in the bed (pressure is higher in the lower parts of the bed).

To overcome this problem the total pressure drop was calculated by dividing the packed bed into a series of smaller packed beds. The computational cell is especially suited for the calculation since all the necessary quantities are known or can be calculated.

Almost all the cell values were extracted and/or calculated from data-files using a data extraction program. The cell gas density was calculated using the ideal gas law and the molar mass of the gas. The cell superficial gas velocity was calculated by multiplying the cell gas velocity with the cell voidage. Calculating the cell superficial gas velocity in this way compensates for pressure decreases and resulting gas velocity increases. The dynamic gas viscosity is assumed constant for the complete bed ($1.8 \cdot 10^{-5}$ kg/m.s) and the particle diameter was 2.5 mm. To avoid potential wall effects, a single column of cells in the middle of the bed was used for calculations. Further on, the three cells nearest to the bottom of the bed and the three cells below the bed surface were not included in the calculations to avoid problems with the calculation of the *local* voidage. This local voidage is the voidage in the direct neighbourhood of a particle and is used for drag calculations. Since the local voidage is calculated from the voidages of the eight neighbouring cells through a volume averaging technique, one wants to have a precise definition of the surrounding cell voidages. Initial concern regarding this strategy resulted

in the use of cells in the middle of the bed. Later on, the pressure drop in the boundary cells was checked and it was found that the initial concern was not grounded.

The particles used in the simulations were positioned in the following manner. The particles were placed very close to each other, resulting in well-defined equal voidage in every cell, with small channels running from bottom to bed surface and horizontal channels across the bed. The resulting voidage was approximately 0.478. A well-defined equal voidage is desired since the pressure calculations make use of the same *local* voidage as mentioned before. If the voidage of every computational cell is the same, the volume averaging technique will use the same *local* voidage for each particle. The results will then be directly comparable with the analytical results of the Ergun equation.

The pressure drop was verified for different gas velocities. In Appendix A, an example will be shown for the system with a superficial gas velocity of 1 m/s. In the table below, simulation parameters and resulting deviations from theoretical pressure drops will be shown. For all cases, the cell dimensions were 1.001x1.001x1.001 cm's. The number of cells in x-, y- and z-direction were 8x8x20 cells. The bed contained 61440 particles, meaning that 15 cell heights were completely filled. The height of the bed that was used for calculations was 11.011 cm.

Case	v_0 (atm) [m/s]	ΔP_{sim} [Pa]	ΔP_{ergun} [Pa]	Dev_{max} [%]	Dev_{mean} [%]	Slip condition
1	1	558.8	558.4	0.09	0.07	Free slip
2	4	6761	6767	0.18	0.09	Free slip
3	10	34768	35050	1.14	0.81	Free slip

Table 6: Pressure drop verification

As can be seen, the deviation from the Ergun equation increases with increasing superficial gas velocity.

§3.3.3 Conclusion

It seems that the interaction between gas and particles for voidages < 0.8 is correctly implemented in the code. The influence of the Ergun equation –used for drag between gas-phase and particles- can indeed be found in the pressure drop. Even for very high superficial gas velocities, the mean deviation between simulation and analytical solutions is only 0.81 percent.

The interaction for voidages > 0.8 was not checked. However, since the implementation of the drag relations for these voidages (Wen&Yu) was already checked in the terminal velocity calculations, it is expected that there will not be significant deviations.

§3.4 Velocity profile in a rectangular bed

§3.4.1 Theory

Verifying the implementation of flowsolver of the z-component of the gas velocity will be done by solving the Navier-Stokes equation in that direction:

$$\rho_g \left[\frac{\partial v_z}{\partial t} + v_x \frac{\partial v_z}{\partial x} + v_y \frac{\partial v_z}{\partial y} + v_z \frac{\partial v_z}{\partial z} \right] = -\frac{\partial p}{\partial z} + \eta \left[\frac{\partial^2 v_z}{\partial x^2} + \frac{\partial^2 v_z}{\partial y^2} + \frac{\partial^2 v_z}{\partial z^2} \right] + \rho_g g_z \quad (30)$$

Some assumptions were made:

- The dynamic viscosity (μ_g) and gas-phase density (ρ_g) are assumed to be constant.
- A stationary situation, so $\partial v_z / \partial t = 0$
- Laminar flow, which means that the flow-lines do not cross each other, resulting in $v_x = 0$ and $v_y = 0$.
- The flow field is established, so no velocity gradients in the z-dimension exist anymore: $\partial v_z / \partial z = 0$ and $\partial^2 v_z / \partial z^2 = 0$.

Using these assumptions, the equation simplifies to:

$$0 = -\frac{\partial p}{\partial z} + \mu_g \left[\frac{\partial^2 v_z}{\partial x^2} + \frac{\partial^2 v_z}{\partial y^2} \right] + \rho_g g_z \quad (31)$$

This can be rewritten to:

$$\frac{-\left(\rho_g g_z - \frac{\partial p}{\partial z}\right)}{\mu_g} = \frac{\partial^2 v_z}{\partial x^2} + \frac{\partial^2 v_z}{\partial y^2} \quad (32)$$

The analytical solution for this type of differential equation was found by *Carslaw* and *Jaeger* [18]. Their basic equation is of the form:

$$\frac{-A_0}{K} = \frac{\partial^2 v}{\partial x^2} + \frac{1}{k^2} \frac{\partial^2 v}{\partial y^2} \quad (33)$$

With the solution (for no-slip conditions):

$$v = \frac{A_0(a^2 - x^2)}{2K} - \frac{16A_0 a^2}{K\pi^3} \sum_{n=0}^{\infty} \frac{(-1)^n \cos[(2n+1)\pi x / 2a] \cosh[(2n+1)\pi ky / 2a]}{(2n+1)^3 \cosh[(2n+1)\pi kb / 2a]} \quad (34)$$

In this equation, a and b are the distances from the centre of the rectangle in x - and y -direction, respectively. The iteration number is n .

The coordinate system used in this equation can be found in figure 11.

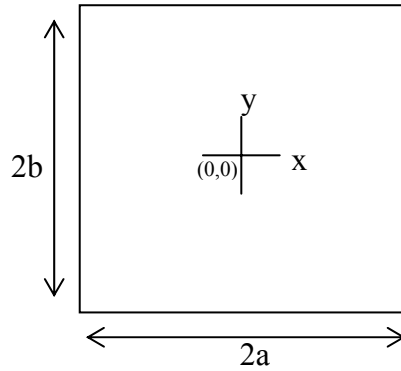


Figure 11: Coordinate system

Solving equation (33) for our situation A_0 , K and k need to be substituted:

$$A_0 = \left(\rho_g g_z - \frac{\partial P}{\partial z} \right) \quad K = \mu_g \quad k = \pm 1$$

Boundary conditions must be applied. For no-slip conditions these are:

$$\begin{aligned} x = \pm a, v_z &= 0 \\ y = \pm b, v_z &= 0 \end{aligned}$$

The differential equation was programmed into C and solved. One hundred iterations were more than enough for the summation to converge.

The result of the program is shown in figure 12.

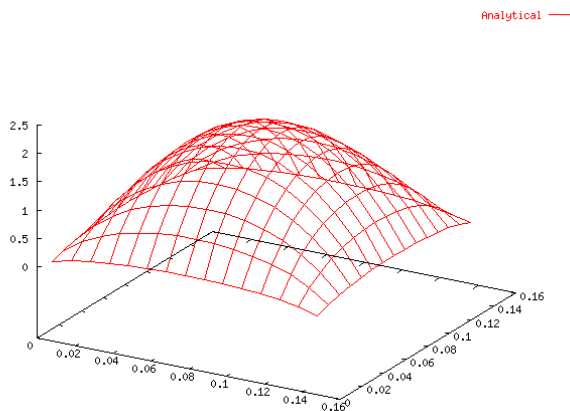


Figure 12: Analytical solution of Navier-Stokes equation

§3.4.2 Results

The pressure drop $\partial P / \partial z$ was obtained from a simulation. A couple of simulations (duration 10 seconds) were carried out using with the following conditions:

Case	X (m)	Y (m)	Z (m)	NX	NY	NZ	<v> (m/s)	η (kg/m.s)	ρ_g (kg/m ³)	Slip
1	0.15	0.15	4.0	15	15	400	1	1.8e-2	1.198	No-slip
2	0.15	0.15	4.0	15	15	400	1	1.8e-2	1.198	Free-slip

Table 7: Simulation conditions

The flow conditions were chosen so that the Reynolds number would remain in the laminar regime ($Re < 2000$), which is important for the assumptions made during the analytical solution of the Navier-Stokes equations. In the following figure, the analytical and model (Case 1) results are plotted:

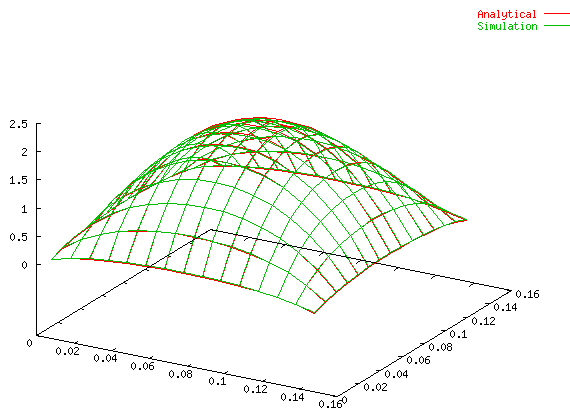


Figure 13: Analytical and model results (Case 1)

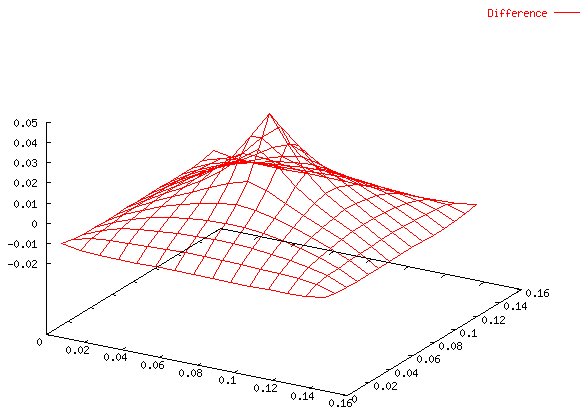


Figure 14: Difference between analytical and model result (Case 1)

The data points near the walls have a higher deviation from the analytical solution than the data points near the centre. Within 0.5 cm of the walls, the deviation in the corners is

about 16 percent and alongside the walls 4 percent. The interior cells show a mean deviation of 0.5 percent. The centre deviates about 2 percent.

Case 2 showed the expected flat profile:

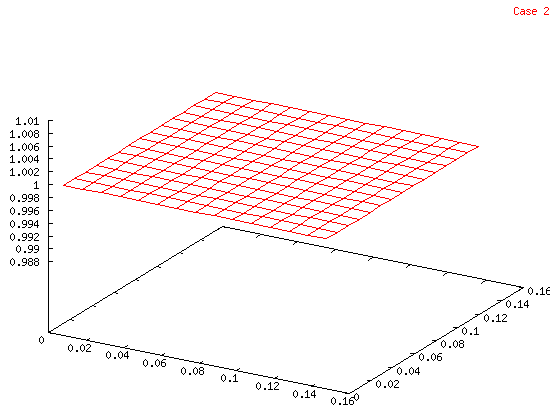


Figure 15: Model results (Case 2)

§3.4.3 Conclusion

From the analytical solution of the Navier-Stokes equations for a rectangular tube and selected simulations, it appears that the Navier-Stokes equations and the boundary conditions are correctly implemented. Applying no-slip to the walls, one finds the expected parabolic velocity profile. Applying free-slip conditions, one finds the expected flat velocity profile.

Some deviations were detected, especially near the walls of the tube. These deviations could amount to 16 percent. For the internal cells, the deviations were usually smaller than 0.5 percent. The assumptions made when solving the Navier-Stokes equations could be responsible for these deviations. Especially the third assumption ($v_x = 0$ and $v_y = 0$) was found not valid for the simulation. For example, in Case 1 the velocities in x- and y-direction were in the order of 10^{-6} - 10^{-10} m/s.

Further on, a steep drop in velocity was found in the region close to the walls. In order to capture these gradients more accurately than in this case, the dimensions of the gridcell should decrease to this order of magnitude (mm's instead of cm's). This was not tested because of the large increase in the number of computational cells.

Chapter 3: Measurement Techniques

§1 Introduction

The discrete particle code can provide information for every model parameter. Since it was unclear which data to use for the validation (and thus to extract during a simulation) an off line analysis tool was developed. The tool uses data files written at certain intervals by the simulation, which were originally used for restarting a simulation after a crash. To this end, these files contain all available information. The tool can be found on the cd-rom that comes with this report.

The data files contain information on the pressure and gas velocity of each computational cell. Also, it contains the position, radius, velocity and rotational velocity of each particle. To validate the model, measurement techniques are needed that can provide quantitative information on the pressure and on the distribution and velocity of the particles.

For model validation of detailed models concerning fluid behaviour, it is very important to use a non-intrusive measurement method. In this manner, the measurement does not affect the fluid and particle behaviour.

In the research group PK-FAP, a novel digital image analysis technique was available. This method (called bubble detection) uses a digital camera (connected to a computer) for data acquisition. Pictures/films obtained by this technique provide quantitative data on (gas) voidages and on bed heights. Using the same pictures/films, another measurement technique in the group -Particle Image Velocimetry (PIV)- was applied. The method provides quantitative information on particle velocities.

A high frequency pressure probe was used to determine the absolute pressure and its fluctuations. The fluctuations give information on bubble behaviour and are thus of great interest. The objective of the pressure measurements is to lay a connection between pressure fluctuations and bedheight fluctuations with as final goal to use pressure fluctuations as a measuring technique for bedheight fluctuations. This technique can then be used to obtain information about bubble behaviour in fluidised beds which can not be analysed using an optical technique (3D beds) anymore like it is used on the pseudo 2D bed this report.

In the following paragraphs, Particle Image Velocimetry, bubble detection and the pressure measurement will be treated in more detail.

§2 Particle Image Velocimetry

§2.1 Introduction

Particle Image Velocimetry (PIV) is an optical (non-intrusive) measurement technique which can provide 2D velocity data for a whole plane in a 3D flow field.

A PIV experimental setup usually consists of a bed constructed from a transparent material. In this bed a light sheet is projected using (for example) a laser or another light source. In order to observe fluid motion the fluid is seeded with tracer material.

The tracer particles must be carefully chosen in order not to influence the flow. They should:

1. exactly follow the motion of the fluid and
2. not alter the flow or the fluid properties and

3. not interact with each other.

When illuminated, the tracer particles can be distinguished and a film of the fluid motion can be recorded using a CCD camera. PIV images can be recorded using different strategies [19]:

1. Single frame / double exposure
2. Single frame / multi exposure
3. Double frame / single exposure

Single frame / double (or higher) exposure means that each frame is exposed twice (or more), such that most particles appear twice (or more) in each image. When using the double frame / single exposure technique, the direction of the displacement can be easily distinguished. In the rest of this introduction a double frame / single exposure example is used.

Usually, the image is analysed by subdividing it into small interrogation regions. Each interrogation region contains particle-image pairs (e.g. the tracer particle on t_1 and the same particle on t_2). Since the displacement can be measured and the time interval is known, the mean particle velocity can be calculated:

$$\bar{\mathbf{v}} = \frac{\mathbf{x}_2 - \mathbf{x}_1}{t_2 - t_1} \quad (1)$$

Calculating the velocity in this manner is called particle tracking and can only be used in fluids with low seed concentration. More specific, the displacement of the tracer particle should be significantly smaller than the distance to the other tracer particles. If this prerequisite is not met, the tracer particles are near each other and one can not be sure

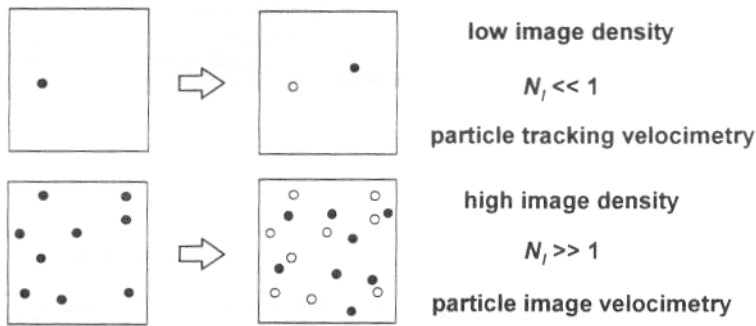


Figure 1: Particle Tracking and PIV

any more which particles form a pair. See figure 1 [20]. In order to obtain more data, higher seeding concentrations are necessary. A problem which arises is the one mentioned before: tracer pairs can not be unambiguously distinguished anymore. It is therefore more convenient to describe the tracer particles in terms of a pattern. One does not call this Particle Tracking anymore, but Particle Image Velocimetry (PIV).

In this report, the double frame / single exposure strategy is followed. Cross-correlation between the images is used to determine the displacements. The equation of the cross-correlation is:

$$R(\vec{s}) = \int I_1(\vec{x})I_2(\vec{x} + \vec{s})d\vec{x} \quad (2)$$

R is the height of the correlation peak, while I_1 and I_2 are the intensities of the particles in the interrogation area of the first and second frame. An example of cross correlation diagram can be found in figure 2 [24]. Imagine having blue tracer particles. The displacement of the blue particles can be determined by multiplying the blue intensity of every particle in the first frame with the blue intensity of every particle in the second frame. Only the displacements of matching particles add up, increasing the height of the correlation peak. The result is the single peak of figure 2.

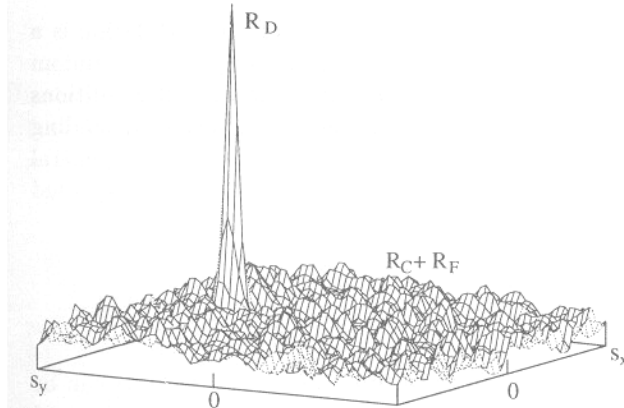


Figure 2: Cross correlation peak

For PIV to deliver meaningful results, the displacement inside an interrogation cell is limited. As a rule of thumb, the displacement in one direction should not be higher than 0.25 times the cell size in the same direction. If the displacement is higher, the chance that parts of tracer patterns leave the interrogation region increases. Patterns leaving the interrogation region cause a decrease in the height of the correlation peak.

§2.2 PIV in the experimental setup

The bed contains 30.000 red particles (diameter 2.5 mm) and 2900 blue tracer particles (diameter 3.0 mm). The reason to use tracer particles with a different diameter was simple: the particle supplier could not supply 2.5 mm particles in the desired blue colour. The requirements with respect to tracer particles as mentioned in §2.1 do not apply to this application of PIV. The blue tracer particles should not significantly change the behaviour of the red particles.

Images of the experimental pseudo 2D setup were recorded using an interlaced 3-CCD camera capturing frames at 25 Hz (which means fields at 50 Hz, see below). The camera is attached to a metal frame and was positioned 65 cm from the bed. Two 500 Watt halogen lamps were positioned on either side of the camera to make a total of four. The camera was positioned in such a way that each blue tracer particle would have a diameter of at least four pixels. In this way, the tracer particles cover both the odd and the even lines (see below).

Since at this distance the area covered by the camera is limited, only the lower part of the bed was studied. For more detailed information, the reader is referred to Chapter 4, paragraph 1.

The interlaced images delivered by the CCD camera can be considered a double frame / single exposure recording strategy. Or rather, double field / single exposure. The interlaced frame consists of exactly two fields. One field is made up of the odd horizontal lines in a frame. This is called the odd field or the top field since it contains the top line of the image. The other field is made up of the even horizontal lines in a frame. This is called the even field or bottom field. See figure 3.

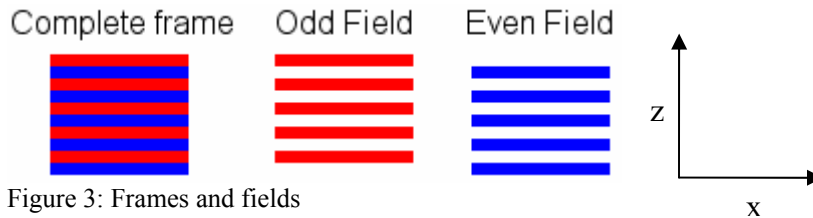


Figure 3: Frames and fields

The two fields are recorded sequentially (time between two fields is $1/50=0.02$ seconds). By splitting the complete frame into the odd and the even field a double field / single exposure (each field is only once exposed) recording strategy is reached.

The PIV analysis software does not identify every single particle in the interrogation region to determine the displacement of the pattern. Rather, it uses cross-correlation (correlation between two fields).

The software multiplies the blue intensity (if using the blue channel) of one pixel in an interrogation region of the first field with the blue intensity of all other pixels in the correlating interrogation region of the second field. If both pixels contain part of a tracer particle (and thus have a relatively high blue intensity), the multiplication delivers a relatively large number. If only one (or none) of the two pixels contains a particle, the multiplication delivers a much lower result. The computer determines which displacement is dominant in the interrogation region. The direction of the displacement is determined automatically since it is known which of two fields was recorded first.

With respect to the correlation of regions: the region in one field is not necessarily compared to a region located at the same position in the other field. If the particle velocities are high enough, the particles will all have left the interrogation region. To reduce this loss of correlation, image shifting is applied. The PIV software first determines the shift of particle patterns using large interrogation regions. In the second run (using small interrogation regions) this shift is used to find the small interrogation region containing the same pattern of particles.

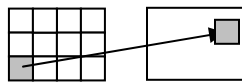


Figure 4: Image shifting

In broad lines, the PIV software follows the following procedure when analysing a recorded frame

1. The blue channel is extracted from the recording.
2. The frame is split into the odd and the even field. The field lines of every field are combined to form two new images: odd and even.

3. Both images are divided into the same large interrogation regions (64x64 pixels). The PIV software is run to determine the shift of particle patterns within these regions. A median check is carried out for a interrogation region using its neighbouring regions. This median check is used to determine the validity of the displacement in one region by comparing it to the median of the displacements of the neighbouring regions. If the displacement differs with more than a certain number of pixels, the displacement being checked is replaced with the median of the displacements of the neighbouring cells. In our case, a factor of 5 pixels was used, meaning that if a displacement deviated more than 5 pixels from the median, it was discarded and replaced. The displacement (in pixels) obtained from this operation is used to for image shifting.
4. The second run is carried out. To this end, the first image is divided into smaller interrogation regions (32x32 pixels). Shift data from the previous run is used to determine the location of the corresponding interrogation region in the second image. Cross-correlation is used to determine the displacement. The image is rotated 90 degrees. Special care must be taken for the displacement in the x-direction. It must be multiplied with 2 and 1 pixel has to be subtracted. This is caused by splitting of the frame into fields.
5. The same median check as in 4. is applied. Now, velocities (in two directions with as unit pixels/sec) are calculated by dividing the displacement in each direction with the time-step between the images.

The area analyzed by the PIV software measured 256 x 608 pixels (or 16 x 38 cells). To maintain compatibility of results, the bubble detection software processed the same area.

§3 Bubble detection

§3.1 Introduction

Bubble detection is an optical (non-intrusive) measurement technique which can provide whole-field information on bubble behaviour. As a result, voidages and bedheights can be calculated accurately. Also, if particles with different colours are used, concentrations can be determined within 10 % accuracy. This feature however was not used in this work. An experimental setup usually consists of a bed constructed from a transparent material. The bed is illuminated by halogen lamps and a digital camera is used to record films.

§3.2 Bubble detection in the experimental setup

Unlike PIV, images used for bubble detection are not split up into odd and even fields since information of a whole field is necessary to determine the voidages.

In broad lines, the bubble detection software follows the following procedure when analysing a recorded frame:

1. The frame is corrected for differences in illumination using a correction field.
2. The blue pixels originating from the blue tracer particles and the red pixels need to be 'translated' to a new intensity (called 'bluered') in order for the bubble detection work properly with the tracer particles. A more detailed description for this procedure can be found below.

3. For every pixel, the intensity is determined. To detect bubbles more accurately, the neighbouring pixels are taken into account too (see below). The averaged 'bluered' intensity of the pixel and its neighbours is compared to the threshold. If the intensity is below the threshold, the pixel is considered a bubble and it gets a green intensity of 255.
4. The pixels with a 'bluered' intensity above a certain threshold are considered to be particles. The pixels below this threshold are considered to be bubbles.
5. Voidages can be calculated for grid cell using: $\varepsilon = 1.0 - 0.6 \left(\frac{\#blueredpixels}{totalpixels} \right)^2$, since even a completely filled grid cell can have no smaller voidage than approximately 0.4
6. Bedheight H can be calculated by using: $H = \frac{\sum H_{blueredpixel}}{\#blueredpixels}$

About 1: The data that is collected for PIV can also be used for bubble detection. However -in contrast to PIV- bubble detection needs a correction field to be able to determine the particle hold-up in a cell. This correction field compensates the differences of illumination on different parts of the bed. This is important, because the particle hold-up is determined using the intensity (between 0 and 255) of the desired colour (red/blue in our case) and lower illumination results in a lower intensity. The correction field is determined by illuminating a homogeneously coloured piece of paper for the duration of 128 frames (a little more than 5 seconds). For each pixel, the average red, green and blue intensities are calculated and saved for later use. The correction factor for a certain pixel is the value of the highest intensity pixel in the whole correction divided by the intensity of that certain pixel in the correction field. The recording of a correction field is repeated at the beginning of each day on which experiments were done.

About 2: For every pixel, a new intensity was calculated. This intensity ensures that the bubble detection also takes the blue particles into account. The new intensity (called bluered intensity) is determined as follows. The bluered intensity for a red particle should be the same as the one for a blue particle. To this end the following equation was solved:

$$xI_{red}^R + yI_{blue}^R = xI_{red}^B + yI_{blue}^B \quad (3)$$

The red plus blue intensity of the red particles (left hand side) should be the same as red plus blue intensity of the blue particles (right hand side). We chose $x = 1$, therefore $y = \frac{I_{red}^R - I_{red}^B}{I_{blue}^B - I_{blue}^R}$. In this case, $y = 113/85$

About 3: The averaging scheme is shown in figure 5. The pixel in question (shaded) receives a weighting factor of 5, the rest of

1	1	1	1	1	← Odd* row
0	0	0	0	0	← Even* row
1	1	5	1	1	← Odd* row
0	0	0	0	0	← Even* row
1	1	1	1	1	← Odd* row

Figure 5: Weighting scheme

the neighbouring cells a factor 1. Only pixels in rows of the same field (see figure 3) are compared. The scheme goes for every pixel on all odd as well as even rows. The denomination 'odd' and 'even' in figure 5 serves only the purpose of example.

About 4: The threshold was determined as follows. A recording was made of the bed without fluidisation. The voidages of all cells were averaged, the result being 0.707. With no particles leaving the area monitored by the digital camera (i.e. the mass balance remains intact), the overall bed voidage must remain the same. The threshold for an experiment satisfying this prerequisite (fluidisation at 2.0 m/s) was adjusted until the bed voidage was approximately 0.707. The resulting threshold of 133 was verified on some other experiments also satisfying the prerequisite and it was found that the average bed voidage was predicted close to 0.707.

About 5: The term $\frac{\#blueredpixels}{totalpixels}$ is squared under the assumption that the particles in the y/z-plane (depth) of the bed show a same hold-up as the x/z-plane (front wall).

§4 Pressure probe

§4.1 Introduction

The pressure probe was used in non-intrusive manner. It was gauged using tubes containing demineralised water. An offset was found and calibration showed that the offset was not constant but changed daily. This is no problem since we are foremost interested in the pressure fluctuations.

§4.2 Pressure probe in the experimental setup

The probe was screwed in the back side (lexan) of the bed in such a way that the inside surface of the wall remained smooth. The connection of the probe with the bed had to be a direct one in order to measure meaningful data at high measuring frequencies (100 Hz). Connection through a tube could buffer the fluctuations. Every experimental situation was carried out three times, so all the three probe positions could be used.

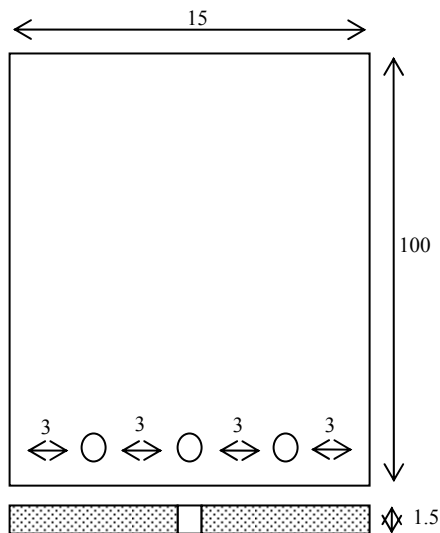
The pressure data were recorded on a dedicated computer through an A/D converter card.

A frequency study of the results was carried out using Fast Fourier Transforms in the computer program Matlab. In short, the Fourier transforms have the ability to identify periodic features. Since the pressure drop (or bed expansion) is expected to be periodical, the Fast Fourier Transform is used to determine the pressure drop/bed expansion frequency. For more details on Fast Fourier Transforms, the reader is referred to [24].

Chapter 4: Experimental

§1 Experimental setup

The experimental setup used for the validation of the discrete particle model (DPM) is a pseudo 2D fluidised bed. The bed measures 15 cm in width, 1.5 cm in depth and 100 cm in height. The relatively small depth is important to keep the number of particles low and to get visible access, needed for the bubble detection. Also, it ensures a relatively small out-of-plane displacement of tracer particles, which is important for PIV analysis. If out-of-plane displacement is high, tracer particles disappear making it more difficult to follow the patterns of tracer particles.



The front of the fluidised bed is made of glass, the back of lexan and the sides of alumina. In the lexan wall three holes have been made for inserting a pressure probe. See figure 1.

The probe is inserted in such a way that the inside surface of the back wall remains smooth.

The gas distributor is split into three sections (left, right and spout) to obtain a good gas distribution. Both the left and right section have two mass flow controllers (500 and 100 litres/min) and the bottom consists of a porous plate (10 μm). The spout section also has two controllers (650 and 20 litres/min) and the bottom consists of metal gauze (0.5 mm)

Figure 1: Rear view and bottom

Facing the bed, a frame is placed to which the 3-CCD camera is attached. To the left and to the right of this frame, halogen lamps (500 W, two on each side) are located (see figure 2).

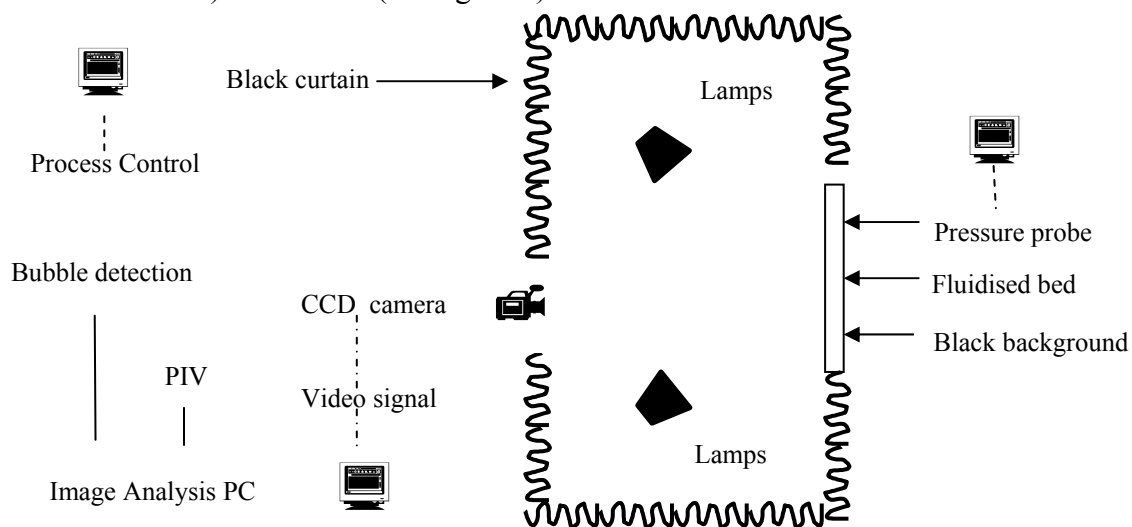


Figure 2: Experimental setup

These lamps illuminate the bed directly in an angle smaller than 45° to avoid reflections to the camera. Behind the bed a black cloth was positioned to provide contrast between particles and bubbles. The rest of the box was clothed in black curtains to eliminate all possible reflections.

To avoid ill behaved fluidisation caused by static electricity, steam is added to the gas flow of the left and the right chamber. The steam is generated in small drums that are placed on heaters. The drums receive demineralised water from a supply vessel, using rotameters for controlled injection. The supply vessel is pressurised at 1 barg to overcome the pressure inside the experimental setup.

The images were recorded using a 3-CCD interlaced digital video camera (JVC KY-F55B) at a frame rate of 25 frames per second, corresponding with 50 fields per second, since the camera is interlaced. The colour components red, green and blue (RGB) are split by a prism and the colour intensity (ranging from 0 to 255) of each individual component is registered on an array of 576×720 pixels. The recorded uncompressed information is bundled into a component video signal that is transferred to a signal converter (Axon ACT-100 bi-directional transcoder). In the transcoder, the signal is converted from RGB to YCrCb, because the frame-grabber is not compatible with the RGB signal from the camera. From the transcoder, it is transferred to the frame-grabber (DPS PVR-3500) where it is stored on a dedicated SCSI hard disk. The data is compressed before storage because the frame grabber can only handle a limited data flow (10 MB/s). The computer containing this equipment is an AMD Athlon system, which is also used to carry out the analyses (bubble detection and PIV). The pressure data were recorded using a pressure probe (Kulite XTC-76A-190M-0.35 barg), capable of high frequency measurements (up to 10 kHz). Measurements were carried out at 100 Hz and recorded on a Pentium PC. For a detailed experimental procedure, see Appendix E.

§2 Experimental and simulation results

§2.1 Introduction

In table 1, all experiments that were carried out are displayed. The experiments were limited by the height of the experimental setup. Experiments that also were simulated in the discrete particle model are marked bold. The minimum fluidisation velocity of the 2.5 mm particles was determined. A value of 1.31 m/s was found, which is in line with velocities reported for previous experiments. See Appendix C for details.

Fluid velocity [m/s]	Spout velocity [m/s]	Fluid velocity [m/s]	Spout velocity [m/s]
1.5	1.5	1	20
2.0	2.0	1	30
2.5	2.5	1.5	20
3.0	3.0	1.5	30
3.5	3.5	1.5	40
		2.0	20
0	20	2.0	30
0	30	2.0	40
0	40	3.0	20
0	50	3.0	30
0	60	Bold experiments were simulated.	

Table 1: Superficial gas velocities of the performed experiments

X_{max}	0.15 m
Y_{max}	0.015 m
Z_{max}	2.00 m
NX	15
NY	1
NZ	200
Slip	Front/back free-slip; left/right no-slip
Coef. of norm. rest.	0.97
Coef. of friction	0.10
Coef. of tang. rest.	0.33
Particle density	2525 kg/m ³
Simulation time	5 sec.

Table 2: Simulation parameters

Due to model limitations only the bold experiments could be simulated. Severe problems are encountered when static situations like for example defluidisation occur. The particles become very closely packed with very low relative velocities. The number of collisions then increases exponentially whilst the impulse exchange concerned with a single collision becomes negligible.

The simulations were performed using 32900 particles with a 2.5 mm diameter. Experiments were carried out using 30000 particles with a 2.5 mm diameter (red), mixed with 2900 particles with a 3.0 mm diameter (blue). The reason to simulate with a different set of particles was the observation that the mixed simulations seemed to take more time. Because time was limited, only simulations with the uniform particle size were performed. The assumption of comparable behaviour was verified by studying the total amounts of kinetic, rotational and potential energy of a particle mix with a uniform particle size. Large differences were not observed. See Appendix D details.

§2.2 Bubble detection

In this paragraph, the results of the bubble detection are presented and discussed. Only two graphs with results are shown, the other graphs can be found in Appendix B.

§2.2.1 Fluidisation results

Fluidisation (and spout) experiments are inherently subject to dynamic fluctuation. In order to compare the voidages from the experiments and the simulations in a meaningful manner, averages were applied. The first step was to calculate a time-average voidage for each cell. This average voidage was calculated for the simulations (125 datasets, 5 seconds) and for the experiments (750 datasets, 30 seconds).

The second step for spouting experiments was vertical averaging, since the spout is a vertical phenomenon, see figure 5. For normal fluidisation, horizontal averaging was applied. The minimum and maximum experimental average voidage of each row was determined and added to the plot, see also figure 3.

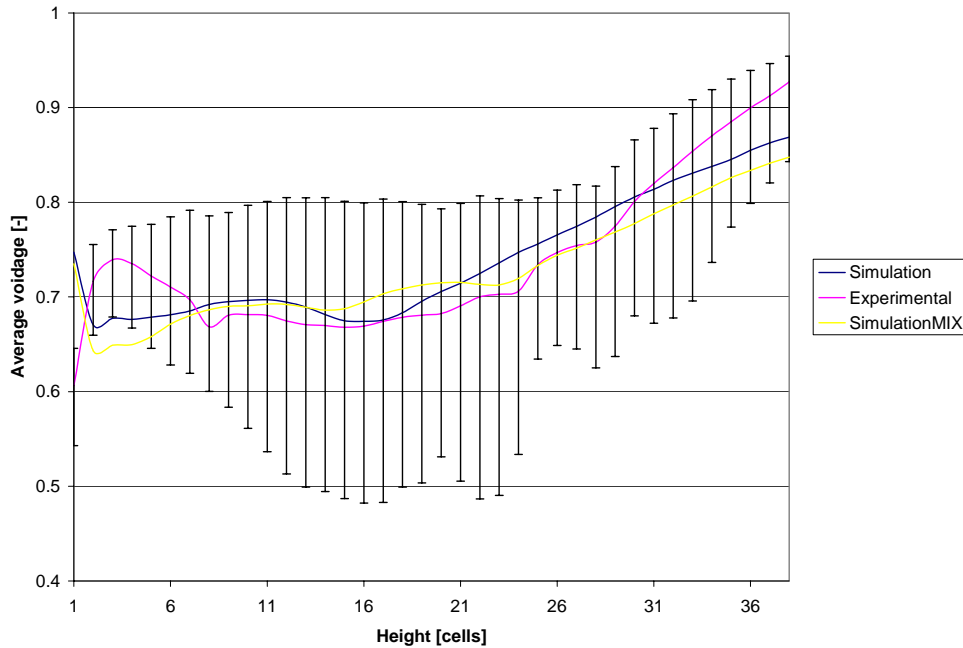


Figure 3: Fluidisation at 3.5 m/s, first experiment

Analysing the figures in Appendix B, it becomes clear that the reproducibility of the experiments is usually within 0.05 voidage. The spread in voidages (figure 3, vertical lines) is caused by the downward flow of solids near the walls. This causes low voidages (high particle hold-up) near the walls and high voidages in the centre of the bed. This is illustrated in figure 4.

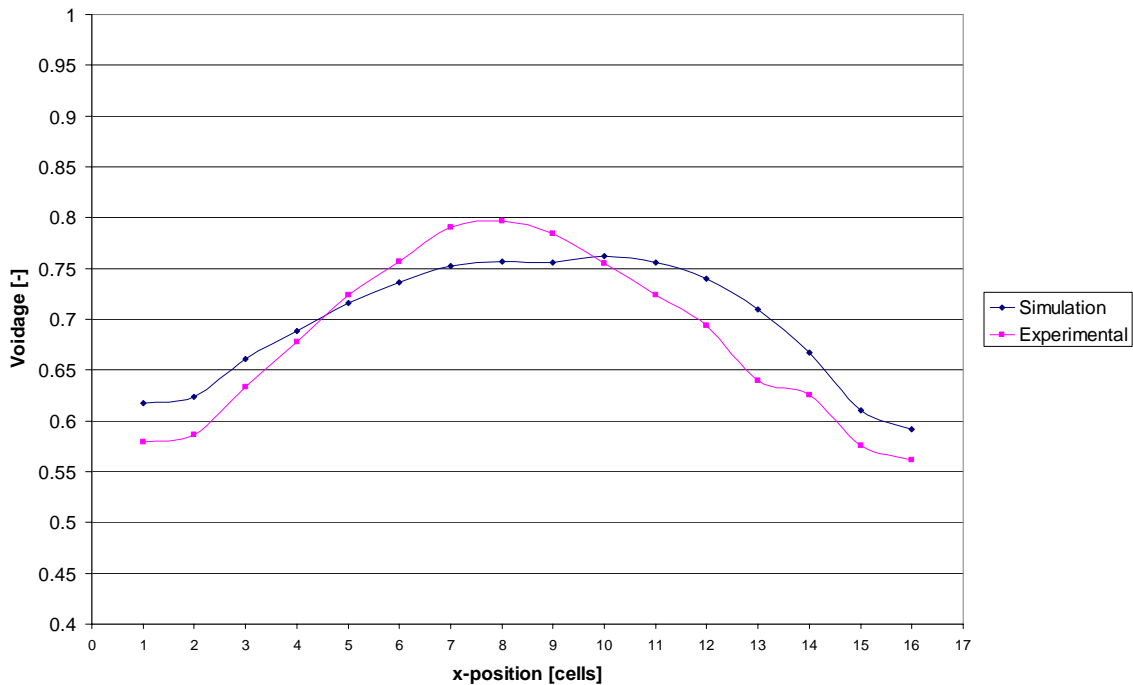


Figure 4: Fluidisation at 3.5 m/s, at a height (cells) of 10

The mean deviation in the voidage between experiment and simulation is calculated (see table 3). In table 3, the number after the ‘F’ is the fluid velocity in dm/s. The number behind the underscore indicates the number of the experiment.

F20_1	0.06	F30_1	0.03
F20_2	0.07	F30_2	0.04
F20_3	0.07	F30_3	0.03
F25_1	0.04	F35_1	0.03
F25_2	0.03	F35_2	0.03
F25_3	0.04	F35_3	0.02

Table 3: Fluidisation; mean voidage deviation

Table 3 shows that the model predicts the voidage of the bed more accurately at higher superficial gas velocities. This could be caused by a better experimental gas distribution at higher velocities. Especially in experiments just above minimum fluidisation (e.g. 1.5 m/s experiments) less ideal experimental gas distribution was observed.

The voidage just above the experimental gas distributor is lower than the second cell. A probable cause for the experimental observation is the formation of slugs, caused by coalescence of the small bubbles rising through particles just above the gas distributor. The bubbles need to a certain distance before they coalesce to a slug.

A phenomenon that occurs in all simulations -but especially at higher gas velocities- is the higher voidage (compared with the second cell) just above the simulated gas distributor. This discrepancy in the simulations is probably caused by the local voidage. The local voidage that is used to calculate the drag force on a particle consists of a weighted average of the voidages of the surrounding cells. The voidage of the gas distributor (0.4) decreases the local voidage significantly, increasing the gas-particle drag. A high drag results in a higher cell voidage in the bottom cells. One can correct this by using the voidage of the cell itself, instead of the bottom voidage. Another solution would be increasing the voidage to a value more reminiscent to the voidage of the porous plate used in the experiment.

§2.2.2 Spouting results

From Appendix B it becomes clear that the reproducibility of the spouting experiments is usually within 0.05 voidage.

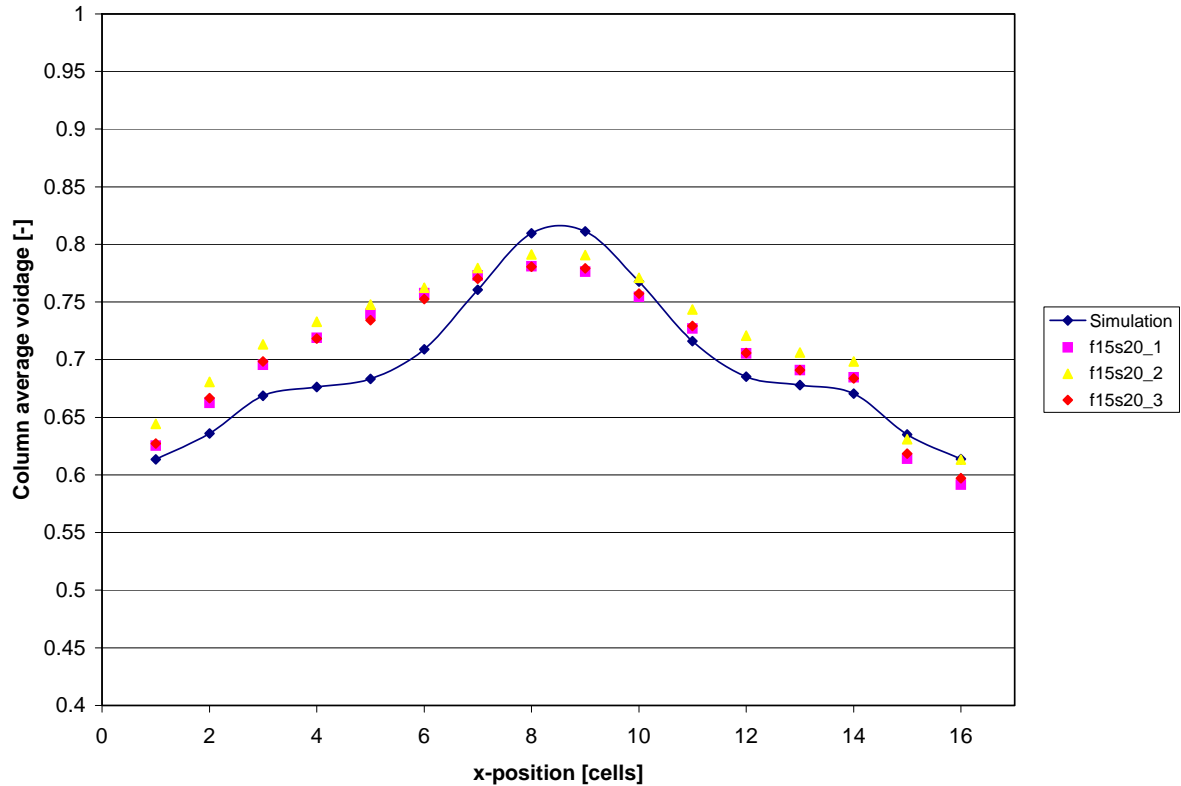


Figure 5: Fluidisation at 1.5 m/s, spout at 20 m/s

The mean deviation between simulation and experiment is calculated. In table 4, the number after the ‘F’ is the fluid velocity in dm/s. The number after the ‘S’ is the spout velocity in m/s. The number behind the underscore indicates the number of the experiment.

F15S20 1	0.03	F20S30 1	0.02
F15S20 2	0.02	F20S30 2	0.03
F15S20 3	0.03	F20S30 3	0.02
F15S30 1	0.05	F20S40 1	0.04
F15S30 2	0.05	F20S40 2	0.05
F15S30 3	0.03	F20S40 3	0.04
F15S40 1	0.02	F30S20 1	0.06
F15S40 2	0.05	F30S20 2	0.06
F15S40 3	0.05	F30S20 3	0.06
F20S20 1	0.02	F30S30 1	0.03
F20S20 2	0.03	F30S30 2	0.06
F20S20 3	0.03	F30S30 3	0.04

Table 4: Spouting; mean voidage deviation

Table 4 shows that the model predicts the voidage of the bed more accurately at a lower overall gas velocity. The cause for this is the erratic behaviour of the spout at high gas

velocities, especially if the background fluidisation is high (e.g. F20S40). The spout seems to prefer blowing to the left side of the bed (this can be seen in the movies), causing a higher voidage on that side and a lower voidage on the right side. In general, the spout behaviour was negatively influenced by a higher background fluidisation.

As can be seen in the figures of Appendix B, the spout experiments show a spout profile that is less clearly outlined than the corresponding simulations. The cause for this is the often erratic behaviour of the spout in the experiments. In simulations, the spout meanders through the bed too, but less erratic. This is illustrated in figure 5. The spout channel is unambiguously located in cell 8 and 9. Application of random effects in the gas distribution should make the simulation behaviour more realistic. One could for example apply a gas inflow with small velocity components in x- and y- direction. The phenomenon of a lower voidage just above the experimental gas distributor first observed in the fluidisation experiments could again be seen in the experimental data of spout simulations.

§2.2.3 Conclusion

The voidage behaviour of the fluidisation experiments compared with the simulations is usually within 0.05 voidage. The reproducibility of the experiments is usually within a 0.05 voidage. The simulations have a better match with the experiments at higher fluidisation velocities. This is probably caused by a better experimental gas distribution at higher velocities.

Some deviations just above the gas distributor could be observed. In simulations, the voidages of the cells just above the distributor (first row) were higher than the ones at the second row. This effect became more profound with increasing gas velocity. The probable cause for this behaviour is the current implementation of the local voidage calculations in the simulation code.

In experiments, the voidages of the cells just above the distributor were much lower than the ones at the second row. A probable cause is the formation of slugs, caused by coalescence of the small bubbles rising through particles just above the gas distributor.

The voidage behaviour of the spouting experiments compared with the simulations is usually within a 0.05 voidage. The reproducibility is approximately the same as the one for the fluidisation experiments. Erratic behaviour of the spout in experiments causes a spout channel that is less clearly outlined than the one in corresponding simulations.

The phenomenon of a lower voidage just above the experimental gas distributor observed in the fluidisation experiments could again be seen in the spout experiments. This also goes for the phenomenon of a higher voidage above the gas distributor in the simulation code.

Application of random effects in the gas distribution would make the simulation behaviour more realistic. One could for example apply a gas inflow with small velocity components in x- and y- direction.

§2.3 Particle Image Velocimetry

In this paragraph, the results of the Particle Image Velocimetry are presented and discussed.

§2.3.1 Fluidisation results

Fluidisation (and spout) experiments are inherently subject to dynamic fluctuation. In order to compare the particle movement from the experiments and the simulations in a meaningful manner, average particle fluxes were used. The flux is defined as

$$f = (1 - \varepsilon) \cdot \mathbf{v}_p \quad (1)$$

with ε the gas voidage and \mathbf{v}_p the particle velocity. Voidages and particle velocities are obtained from the same experiments. Voidages using bubble detection and particle velocities using PIV.

The PIV software comes with some statistical software. The software is able to calculate average velocities for every cell. It can also provide the average RMS (root mean square) values. The RMS value is important in the respect that it gives an indication of the bed dynamics. Large RMS values indicate large fluctuations of the studied parameter. The average velocity is calculated using:

$$\bar{v} = \frac{1}{N} \sum_{i=1}^N v_i \quad (2)$$

and its RMS value using:

$$v' = \sqrt{\frac{1}{N^2} \sum_{i=1}^N (v_i - \bar{v})^2} \quad (3)$$

N is the number of data points. For simulations, this is 125 and for experiments 750. Average particle fluxes and its RMS values can be calculated using the same set of equations.

From simulation velocities, maximum and minimum particle velocities in the z-direction were obtained. To determine if a PIV analysis would be meaningful, the maximum and minimum displacement was determined. The displacements can be found in table 5:

Fluidisation velocity [m/s]	Minimum average particle velocity [m/s]	Maximum average particle velocity [m/s]	Maximum displacement [pixels]
2.0	-0.56	0.22	19
2.5	-0.82	0.31	27
3.0	-1.03	0.41	34
3.5	-1.01	0.46	33

Table 5: Maximum displacements, obtained from simulations

The interrogation region that is used for image shifting measures 64x64 pixels. Table 5 shows that none of the particle velocities satisfy the prerequisite of a displacement of

only $0.25 \cdot 64 = 16$ pixels (see chapter 3, paragraph 2.1). The PIV software was still used and it was kept in mind that the results could be unreliable.

To get an indication of the validity of the PIV data, the influence of the median check was studied. This was done by comparing the number of cells which were adapted by the median check with the total number of cells. The results are in table 6.

Experiment	1	2	3
2.0 m/s	48 %	44 %	48 %
2.5 m/s	66 %	66 %	66 %
3.0 m/s	74 %	74 %	74 %
3.5 m/s	79 %	79 %	78 %

Table 6: Rejected vectors

From table 6 it becomes clear that only little value can be given to the results. Therefore, it was only tried to get qualitative data from the results.

The two vector diagrams in figure 6 show the fluxes for 2.0 m/s fluidisation. The axes were made dimensionless by dividing through the bed width (15 cm).

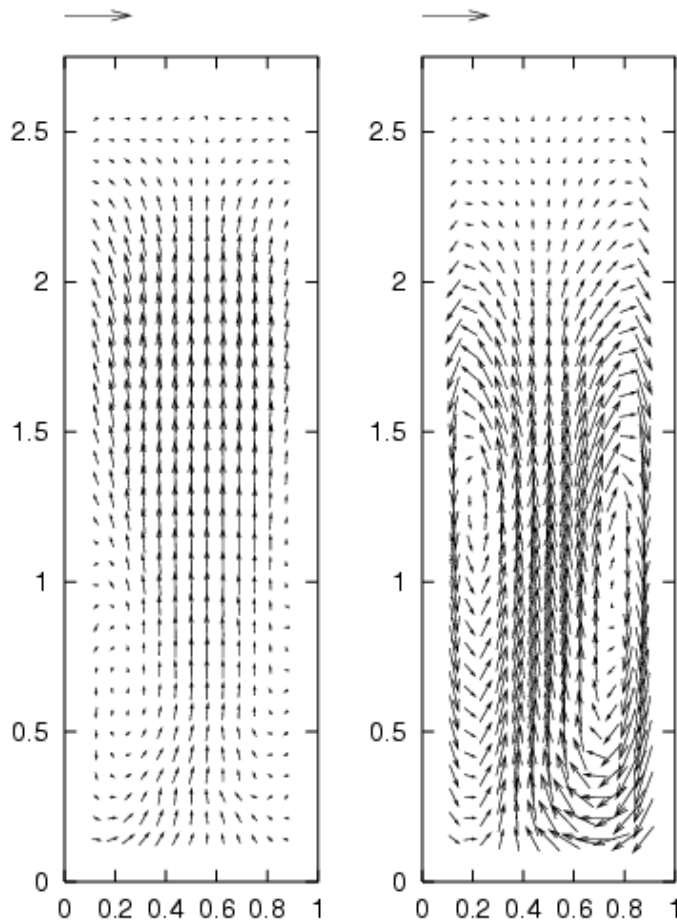


Figure 6: Left-hand side: flux obtained from PIV, right-hand side flux obtained from simulation

The arrow at the top of the pictures is provided for scaling and measures 0.13 m/s (10 % of the minimum fluidisation velocity). Figure 6 shows the experimental flux is for the largest part directed upward. Also, the fluxes seem smaller in the bottom side of the bed. The pictures and data for the other fluidisation experiments and simulations can be found on the cd-rom.

In the following three figures, the experimental data of the experiment is compared with the simulation results. Average particle fluxes (in the z-direction) were plotted for the simulation as well as the corresponding experiments at three different heights.

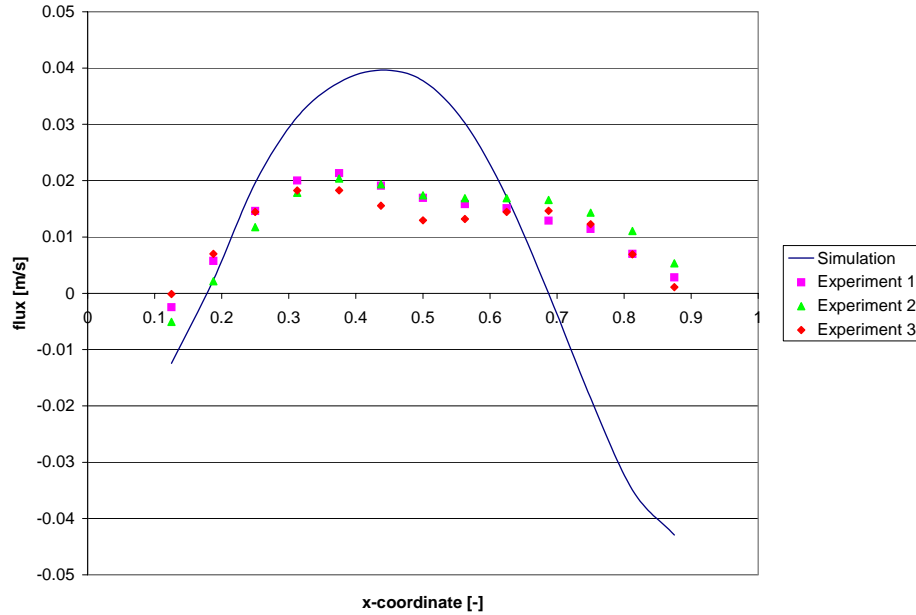


Figure 7: z-fluxes at z-coordinate of 0.14

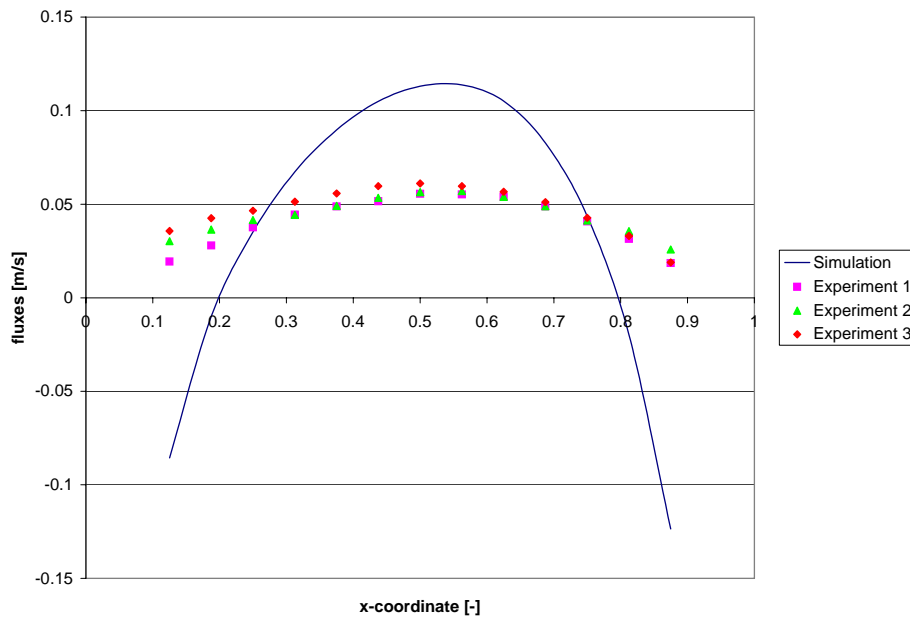


Figure 8: z-fluxes at z-coordinate of 1.34

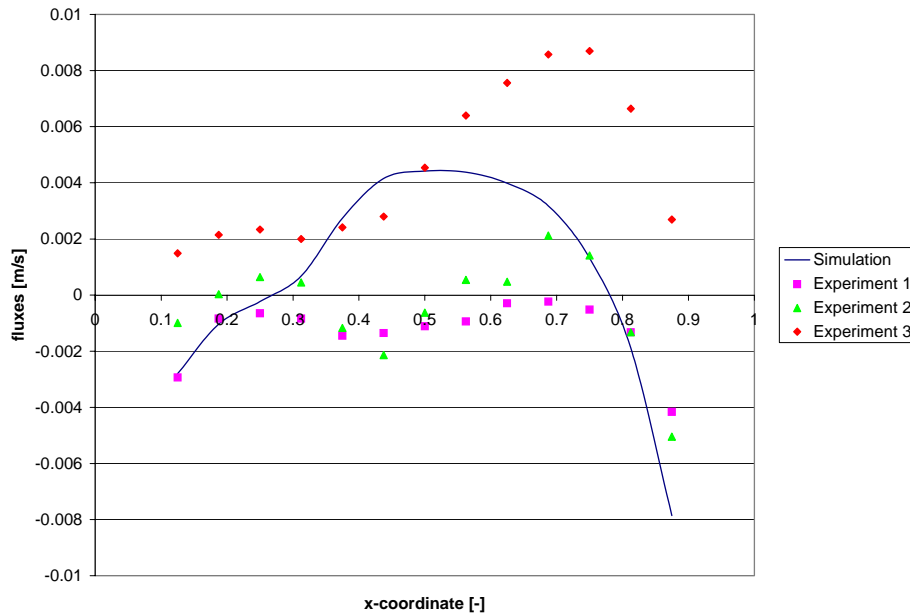


Figure 9: z-fluxes at z-coordinate of 2.54

The simulations show high particle fluxes in the middle of the bed and lower ones near the walls. However, the fluxes near the walls were not found to be directed downward, as can be seen in the simulations. One reason could be the relatively sharp transition of positive to negative fluxes as shown in simulations. Because of this sharp transition, velocities directed up and downward can be found in the same interrogation region, making it difficult to determine the correct-displacement peak in the cross-correlation diagram.

A couple of RMS pictures of the simulated 3.0 m/s fluidisation case discussed below can be found in Appendix G. More can be found on the cd-rom.

During the investigation of the RMS values for the simulation x- and z-flux some trends were discovered. With increasing height, the RMS value for the x-flux decreased. This indicates that the x-fluxes fluctuate less with increasing height. This seems logical since the particles are almost at the highest point of their trajectory. They will primarily move from the centre of the column to the left and right wall with little fluctuations. The largest fluctuations occur in the lower part of the bed. It could be possible that the large fluctuations in the lower part of the bed are caused by the rising of bubbles. When the bubble rises up through the bed, it ‘sucks’ particles in its wake, effectively inducing horizontal transport of particles from the left and right wall to replace the particles. If this is the case, perhaps following the RMS for the x-flux value just above the porous plate could give information on the rate of bubble formation. In experiments, a similar trend could be observed but because of the unreliability of the data no conclusions in this respect were drawn.

The RMS values in simulations for the z-flux increases to a maximum (before decreasing) with increasing height. This indicates that the z-fluxes fluctuate more with increasing height. It is expected that these larger fluctuations too are caused by bubbles

rising up through the bed. Studying the fluidisation simulations, it could be seen that at a certain location in the middle of the bed particles move upward in front of a bubble (positive flux). When the bubble passes the location, particles 'rain' downward (negative flux). These phenomena cause large fluctuations with respect to the average flux on that position. In experiments, a similar trend could be observed but because of the unreliability of the data no conclusions in this respect were drawn.

§2.3.2 Spouting results

The problem of large particle displacements that played in the fluidisation experiments is of even greater importance in spout experiments, since particles in the spout obtain even higher velocities than the ones in table 5. According to the simulations, particles in the spout obtain velocities up to 3 m/s (at a spout velocity of 40 m/s). The displacement of the particles in the time interval is 0.06 m (or 99 pixels). If the demand that the interrogation region is approximately four times the particle displacement were applied, one would find that an interrogation region of approximately 400x400 pixels is required. Even applying a less strict demand would still give a 200x200 pixel interrogation region. This region is far too large to determine a displacement accurately since particles in this region will probably not be moving in one single direction, making it more difficult to determine the correct peak in the cross correlation diagram.

If one wants to apply PIV to a spouted bed, a camera with a much smaller recording interval between frames/fields is necessary. For the spout velocity of 40 m/s, a time of 1 or 2 ms should work (current camera has 20 ms).

§2.3.3 Conclusion

With the current camera equipment, PIV could not be carried out for spout experiments and its application to normal fluidisation was also limited to cases with very low (near minimum fluidisation) superficial gas velocities.

§2.4 Pressure measurements

In this paragraph, the results of the pressure measurements are presented and discussed. A few selected cases will be shown, to provide ‘proof of principal’ with respect to a coupling between pressure fluctuations and bedheight fluctuations. The experimental and simulation data are analysed using Fast Fourier Transforms in Matlab to determine pressure and bedheight fluctuations.

§2.4.1 Bedheight and pressure fluctuations

To determine the coupling between bedheight and pressure fluctuations in the experiment, data has to be available for both. Since the camera was positioned very close to the bed for PIV analysis, only a few experiments retained all the particles within the view of the camera. All the particles must be in view to calculate the bedheight accurately.

Frequency results for the experiments meeting the conditions mentioned above are shown in table 7 and 8. The pressures were recorded on three positions: “left”, “spout position” and “right”, except for the fluidisation experiments. These three positions are measured in three separate experiments. If multiple frequencies are shown, they are arranged with the strongest correlation peak first, the second strongest in parentheses.

Velocity		Right 1	Right 2	Right 3
1.5 m/s	<i>Bedheight</i>	1.5	1.8	1.5 (1.9)
	<i>Pressure</i>	1.5	1.7 (1.9)	1.9 (1.5)
2.0 m/s	<i>Bedheight</i>	1.7	1.6	1.6
	<i>Pressure</i>	1.7	1.6	1.6

Table 7: Experimental fluctuation frequencies [Hz]

Velocity		Left	Spout position	Right
1.0/30 m/s	<i>Bedheight</i>	4	4	4 (1.8)
	<i>Pressure</i>	4	4	4
1.5/20 m/s	<i>Bedheight</i>	2.2 (2.6)	1.6 (2.1)	2 (2.2)
	<i>Pressure</i>	2.6 (2.2)	1.7	2 (2.8)

Table 8: Experimental fluctuation frequencies [Hz]

Velocity		Overall
2.0 m/s	<i>Bedheight</i>	1.6 (1)
	<i>Pressure</i>	1.6 (1.2)
2.5 m/s	<i>Bedheight</i>	1
	<i>Pressure</i>	2.6 (2.2)
3.0 m/s	<i>Bedheight</i>	1.2 (1.8)
	<i>Pressure</i>	1.2 (1.6)
3.5 m/s	<i>Bedheight</i>	1.2 (2.2)
	<i>Pressure</i>	2.2
3.5 m/s MIX	<i>Bedheight</i>	1.4 (0.6)
	<i>Pressure</i>	1.4

Table 9: Simulation fluctuations frequencies [Hz]

In Appendix F, the frequency and fluctuation spectra are shown for the experimental case of 2.0 m/s. The other spectra can be found on the cd-rom.

The data in tables 7 and 8 clearly shows the connection between bedheight and pressure fluctuations. Table 9 shows some connection, but the amount of simulation data was not

sufficient. The spout experiment in table 8 shows a lower fluctuation frequency in the centre of the bed, probably due to presence of the spout. Perhaps, the frequency indicates the rate in which the spout collapses.

To further investigate the coupling between experiments and simulations, longer simulations are required to obtain stronger peaks in a Fourier analysis. With respect to experiments, more bedheight - pressure drop correlation can be obtained by positioning the camera further from the bed.

§2.4.2 Comparing simulation and experiment

Velocity	Simulation	Experimental		
		Left	Spout position	Right
2.0 m/s	1.6 (1.2)	1.7	1.6	1.6
2.5 m/s	2.6 (2.2)	1.4	1.4 (1.3)	1.4 (1.5)
3.0 m/s	1.2 (1.6)	1.2 (1.6)	1.1 (1.2)	1.1
3.5 m/s	2.2	2.5 (2.4)	2.4 (1.3)	1.1 (0.9)

Table 10: Experimental and simulation pressure fluctuation frequencies [Hz]; fluidisation

Velocity		Left	Spout position	Right
1.5/20 m/s				
Simulation	<i>Bedheight</i>	1.2	2.4 (2.8)	1.2
	<i>Pressure</i>	2.6 (5.4)	2.6 (5.4)	2.6 (5.4)
Experiment	<i>Bedheight</i>	2.2 (2.6)	1.6 (2.1)	2 (2.2)
	<i>Pressure</i>	2.6 (2.2)	1.7	2 (2.8)

Table 11: Experimental and simulation fluctuation frequencies [Hz]; spout

The results from table 10 and 11 indicate that simulation start-up effects probably still have a too profound effect on the bed dynamics. Although dump-files (start-up files for simulations) of comparable simulations were used to start the simulation (causing lower initial disturbances), still some start-up effects can be recognised. Also, more experimental measurements at the same bed position would give a better indication of the bed fluctuations.

Of the experiments, only fluidisation at 2.0 and 2.5 m/s provides unanimous bed fluctuation frequencies (1.6 Hz and 1.4 Hz). Fluidisation at 3.0 m/s indicates a fluctuation of 1.23 Hz or 1.07 Hz, while fluidisation at 3.5 m/s does not give any clear information. Comparing the experimental frequency data of 2.0 and 2.5 m/s with Goldschmidt [25], no deviations were detected. Goldschmidt obtained fluctuations of 1.6 Hz and 1.4 Hz for 1.9 and 2.5 m/s experiments, respectively.

The results of table 11 show some comparable pressure frequencies in the left and right of the bed between simulation and experiment, but the spout frequency is different.

Mean absolute pressures drops of simulation and experiment were compared (table 12).

Velocity	Simulation	Experimental (probe)	Experimental (manometer)
2.0 m/s	2.9 kPa	4.6 kPa	3.0 kPa
2.5 m/s	2.9 kPa	4.7 kPa	3.0 kPa
3.0 m/s	2.9 kPa	4.8 kPa	3.0 kPa
3.5 m/s	3.0 kPa	4.8 kPa	3.0 kPa

Table 12: Mean absolute pressures drops

Table 12 shows that the pressure probe provides an 18 kPa offset. Calibrations showed that the offset was not constant but changed daily. Perhaps, the atmospheric pressure has an influence on this. Comparing the manometer with the simulations, it seems that the simulation predicts the average pressure drop accurately.

One can also see that increasing gas velocities beyond the minimum fluidisation velocity has only small effect on the pressure drop, as can be expected.

§2.4.3 Conclusion

Investigation of experimental bedheight and pressure fluctuations indicates that a coupling between these fluctuations exists. This goes for normal fluidisation as well as spout fluidisation.

Comparison of experiments and simulations is not possible because of the amount of simulation data. Longer simulation times are necessary to get clearer results with the Fourier analysis.

Fluidisation experiments of 2.0 and 2.5 m/s showed a good agreement with Goldschmidt. The spouting experiment fluctuations in left and right sections of the bed were comparable with the simulations. The spout showed a lower fluctuation than the one predicted by the simulation, but more experimental data is required to make a conclusive judgement on this observation.

The simulations accurately predicted the absolute pressure drop for normal fluidisation.

Chapter 5: Conclusions and recommendations

In this report, the discrete particle model developed in the research group PK-FAP was verified and validated. Verification encompassed the ‘verification’ of the implementation of key model equations. These are the gas-solid drag equations and the gas-phase hydrodynamics.

The Wen&Yu equation ($\varepsilon > 0.8$) was verified using the terminal velocity of a falling particle. Both the Newton ($Re \geq 1000$) and intermediate region ($Re < 1000$) were properly implemented. The Newton region showed a deviation in the eventual terminal velocity of 0.024 % and the intermediate region one of 0.033 %. The Stokes region ($Re < 0.1$) showed a deviation of 2.47 %. This was caused by implementation of the Wen&Yu equations. If the Stokes equation was applied, a deviation of 0.048 % was found.

The Ergun equation ($\varepsilon < 0.8$) was verified using the pressure drop over a packed bed. Deviations for superficial gas velocities of 1 m/s and 4 m/s were below 0.10 %. At 10 m/s, a deviation of 0.81 % was found.

The gas-phase hydrodynamics (Navier-Stokes equations) were verified by comparing the z-velocity profile from a simulation with the profile obtained from the analytical solution. It was found that the Navier-Stokes equations were properly implemented. Deviations were smaller than 0.5 % for the centre of the column. Near the walls, the deviation amounted up to 16 %, caused by the steep velocity gradient near the wall.

The validation was performed through experiments in a pseudo 2D (spout-) fluidised bed. Voidages were obtained through an imaging technique called bubble detection, particle fluxes through particle image velocimetry and pressure fluctuations from a high frequency pressure probe.

The voidage behaviour of the fluidisation and spout experiments compared with the simulations is usually within 0.05 voidage resemblance.

With the current camera equipment, particle image velocimetry could not be carried out for spout experiments and its application to normal fluidisation was also limited to cases with very low (near minimum fluidisation) superficial gas velocities.

Investigation of bedheight and pressure fluctuations using the high frequency pressure probe indicates that a direct coupling between these fluctuations exists. This goes for normal fluidisation as well as spout fluidisation. Comparison of experiments and simulations was not possible. Longer simulation times are necessary to get clearer results with the Fourier analysis. Fluidisation experiments of 2.0 and 2.5 m/s showed a good agreement with Goldschmidt. The simulations accurately predicted the absolute pressure drop for normal fluidisation.

Recommendations

Experimental

- The threshold for bubble detection should be determined at the beginning of every day of experiments, using the procedure mentioned in chapter 3, paragraph 3.2.
- An experiment without tracer particles should be carried out to determine if the tracers influence bed behaviour. Simulations did not show large deviations, but perhaps experiments will.
- The particle velocities determined by the PIV software should be validated using the rotating disk method available in this group. Preliminary results of PIV using old rotating disk experiments (mix of 1.5 and 2.5 mm particles) indicate no problems. However, it is necessary to carry out validation with the particles used in these experiments (2.5 and 3.0 mm).
- The PIV experiments should be recorded using a non-interlaced digital camera that can record images within 1 or 2 ms after each other. With these small time steps, the displacement of the particles is small enough for PIV to give meaningful results.
- The interrogation areas used by PIV should be as small as possible to correctly capture the sharp velocity gradients caused by rising and falling particles. This could be done if a better digital camera (see previous recommendation) is available.
- More experiments with respect to the coupling between pressure drop and bedheight should be carried out. To this end, the complete bed should be recorded (instead of half the bed, as in this report). Experiments to be carried out should at least include normal fluidisation in the range 1.5-3.5 m/s.
- The pressure probe has an off-set that changes on a daily basis. It is recommended that the manufacturer is contacted for investigation.
- The application of lexan in the bed could influence the collision parameters to be used in the computer model. It is recommended to at least determine the coefficient of restitution.
- A steam facility should be added to the spout section in the pseudo 2D bed.

Simulation

- The gas distribution in simulations is ‘perfect’. This usually results in highly symmetrical but unrealistic profiles, see for example the voidage profile of the spouting experiment in chapter 2, paragraph 2.2.2. To obtain a more realistic gas distribution, one could introduce in the gas inflow small (random) velocity components in the x- and y-direction.
- In the future, longer simulation times are required to better capture periodical phenomena. Comparing time-averaged particle fluxes for example does not give an overall particle flux of zero (“what goes up, must come down”). Perhaps this particle flux would be a good indication when to finish the simulation. Longer simulations will probably also improve the results of the Fourier analysis performed on bedheight and pressure fluctuations.
- The local voidage for particles in the cells just above the gas distributor should be calculated in a different manner. The current implementation results in higher cell voidages above the distributor. One option is to use the voidage of the cell itself for the volume averaging, instead of the bottom voidage. Another solution would be increasing

the bottom voidage to a value more reminiscent to the voidage of the experimentally used porous plate.

- The flowsolver should be checked to determine the cause of the strange fluctuations in the terminal velocity when using multiple cells in the z-direction (see chapter 2, paragraph 3.2.3).

- In order to simulate closely packed beds with very low relative particle velocities, the hard- sphere collision model does not suffice. A soft-sphere collision model would be well suited for these situations. Perhaps a hybrid code, employing the soft-sphere model for dense regions and the hard-sphere model for the rest of the bed, could be developed.

Literature

1. B.P.B. Hoomans, *Granular Dynamics of Gas-Solid Two-Phase Flows*, Ph.D. Thesis University of Twente, 1999, ISBN 90-36514010
2. D. Kunii, O. Levenspiel, *Fluidization Engineering second edition*, Butterworth-Heinemann, Newton (MA), 1991, ISBN 0-409-90233-0
3. M.J. San Jose, M. Olazar, M.A. Izquierdo, S. Alvarez, J. Bilbao, *Spout Geometry in Shallow Spouted Beds*, Ind. Eng. Chem. Res. 40 (2001), p. 420-426
4. J.Y. Day, M.H. Morgan, H. Littman, *Measurements of spout voidage distributions, particle velocities and particle circulation rates in spouted beds of coarse particles – II Experimental Verification*, Chem. Eng. Sci 42 (1987), p. 1461-1470
5. M. Olazar, M.J. San Jose, A. T. Aguayo, J.M. Arandes, J. Bilbao, *Design factors of conical spouted beds and jet spouted beds*, In. Eng. Chem. Res. 32 (1993), p. 1245-1250
6. M. Olazar, M.J. San Jose, M.A. Izquierdo, S. Alvarez, J. Bilbao, *Local Bed voidage in spouted beds*, Ind. Eng. Chem. Res. 40 (2001), p. 427-433
7. M. Olazar, M.J. San Jose, A.T. Aguayo, J.M. Arandes, J. Bilbao, *Stable operation conditions for gas-solid contact regimes in conical spouted beds*, Ind. Eng. Chem. Res. 31 (1992), p. 1784-1792
8. C. Heil, *Some Properties of Spout-Fluid Beds*, Ph. D. Thesis Eindhoven University, 1984
9. A. Nagarkatti, A. Chatterjee, *Pressure and Flow Characteristics of a Gas Phase Spout-Fluid Bed and the Minimum Spout-Fluid Condition*, Can. J. Chem. Eng. 52 (1974), p. 185-195
10. O. Uemaki, T. Tsuji, *Particle velocity and solids circulation rate in a jet-spouted bed*, Can. J. Chem. Eng. 70 (1992), p. 925-929
11. M. Olazar, M.J. San Jose, A.T. Aguayo, J.M. Arandes, J. Bilbao, *Hydrodynamics of nearly flat base spouted beds*, Chem. Eng. J. 55 (1994), p. 27-37
12. D.L. Pianarosa, L.A.P. Freitas, C.J. Lim, J.R. Grace, O.M. Dogan, *Voidage and particle velocity profiles in a spout-fluid bed*, Can. J. Chem. Eng. 78 (2000), p. 132-142
13. Y.L. He, C.J. Lim, S.Z. Qin, J.R. Grace, *Spout diameters in full and half spouted beds*, Can. J. Chem. Eng. 76 (1998), p. 702-706
14. Y.L. He, C.J. Lim, J.R. Grace, *Pressure gradients, voidage and gas flow in the annulus of spouted beds*, Can. J. Chem. Eng. 78 (2000), p. 161-167
15. M. Z. Anabtawi, B. Z. Uysal, R.Y. Jumah, *Flow characteristics in a rectangular spout-fluid bed*, Powder Techn. 69 (1992), p. 205-211
16. M.B. Saidutta, D.V.R. Murthy, *Mixing behaviour of solids in multiple spouted beds*, Can. J. Chem. Eng. 78 (2000), p. 382-385
17. D. Geldart, Powder Techn. 7 (1973), p. 285
18. H.S. Carslaw, J.C. Jaeger, *Conduction of heat in solids*, Clarendon Press, Oxford, 1959
19. J. Westerweel, *Fundamentals of digital particle image velocimetry*, Meas. Sci. Technol. 8 (1997), p. 1379-1392
20. J. Westerweel, *PIV introduction course*, Delft University of Technoly, june 2000
21. N.G. Deen, J. Westerweel, E. Delnoij, *Two-phase PIV in bubbly flows: status and trends*, Chem. Eng. Technol. 25 (2002) 1, p. 97-102

22. S. Mellema, *Ontwikkeling van een meetmethode voor segregatie in gas-gefluidiseerde bedden met behulp van digitale beeldanalyse*, Graduation Thesis University of Twente, 1999
23. G.J. Borse, *Numerical Methods with MATLAB – a resource for scientists and engineers*, PWS Publishing, Boston, 1997
24. M. Raffel, C. Willert, J. Kompenhans, *Particle Image Velocimetry – a practical guide*, Springer-Verlag, Berlin, 1998
25. M. Goldschmidt, *Hydrodynamic modelling of fluidised bed spray granulation*, Ph.D. Thesis University of Twente, 2001, ISBN 90-36516374

List of symbols

c_d	drag coefficient, [-]
d_p	particle diameter, m
\mathbf{F}	force, N
\mathbf{g}	gravity, m/s^2
$I_{a,b}$	moment of inertia, $kg.m^2$
\mathbf{J}	impulse vector, $kg.m/s$
L	length of packed bed, m
$m_{a,b,p}$	particle mass, kg/m^3
M_g	molecular mass (air: 0.0288), kg/mol
\mathbf{n}	normal unit vector, [-]
N_x, N_y, N_z	number of computation cells in x-, y- and z-direction, [-]
P	pressure, N/m^2
R	gas constant (8.314), $J/kg.K$
$R_{a,b}$	particle radius, m
Re_p	particle Reynolds number, [-]
$\mathbf{r}_{a,b}$	particle position, m
S_p	momentum exchange source term, $kg/m^2.s^2$
t	time, s
T	temperature, K
\mathbf{u}	gas-phase velocity, m/s
$\mathbf{v}_{a,b,p}$	particle velocity, m/s
V_p	particle volume, m^3
X_{max}	column dimension in x-direction, m
Y_{max}	column dimension in y-direction, m
Z_{max}	column dimension in z-direction, m

Greek symbols

β	interphase momentum exchange coefficient, $kg/m^3.s$
ε	voidage, [-]
λ_g	gas-phase bulk viscosity, $kg/m.s^2$
μ_g	gas shear viscosity, $kg/m.s$
ρ_g	gas-phase density, kg/m^3
ρ_p	particle density, kg/m^3
$\boldsymbol{\tau}_g$	gas phase stress tensor, $kg/m.s^2$
$\omega_{a,b}$	angular velocity, 1/s

Appendix A: Pressure drop calculation

Appendix B: Bubble detection results

Part 1: Fluidisation

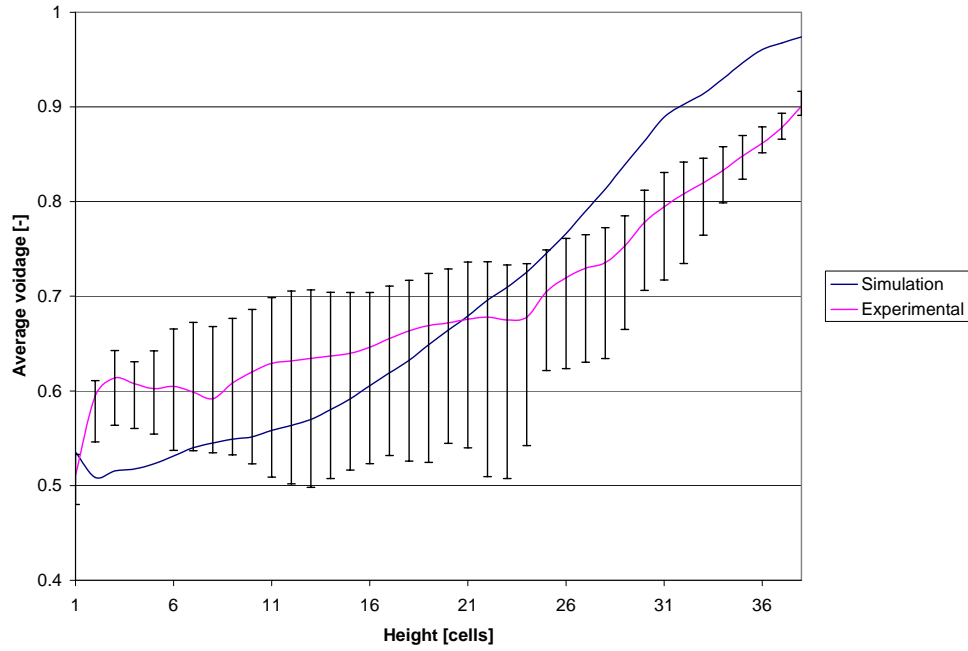


Figure 1: Fluidisation at 2 m/s, first experiment

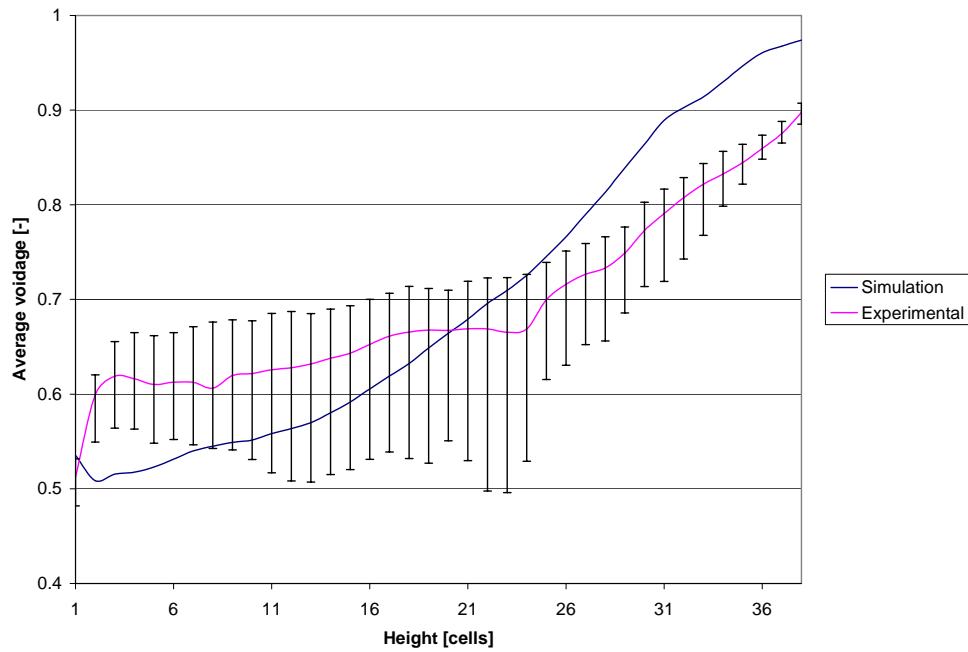


Figure 2: Fluidisation at 2 m/s, second experiment

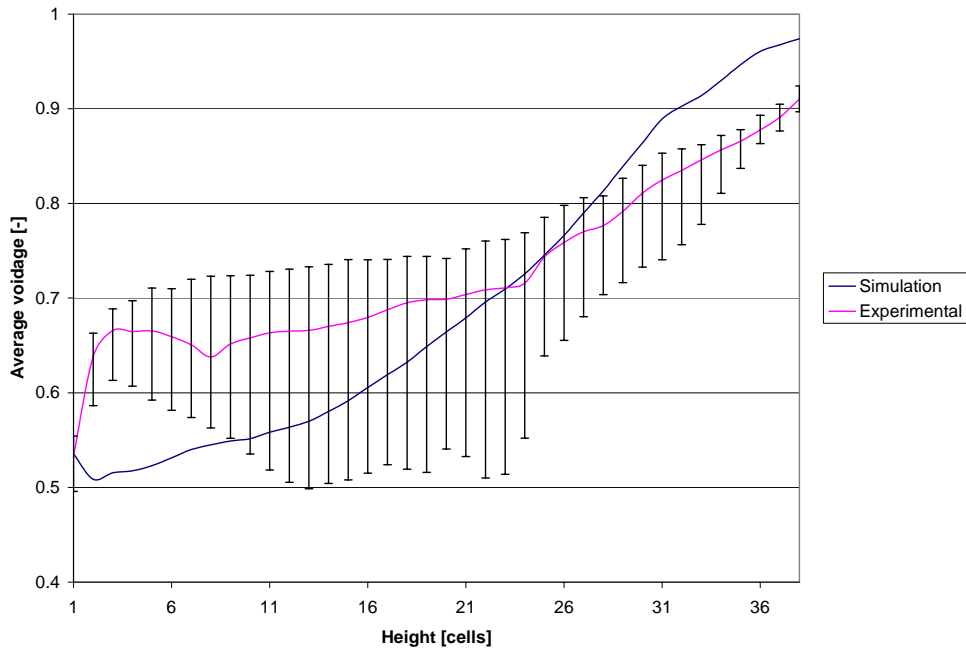


Figure 3: Fluidisation at 2 m/s, third experiment

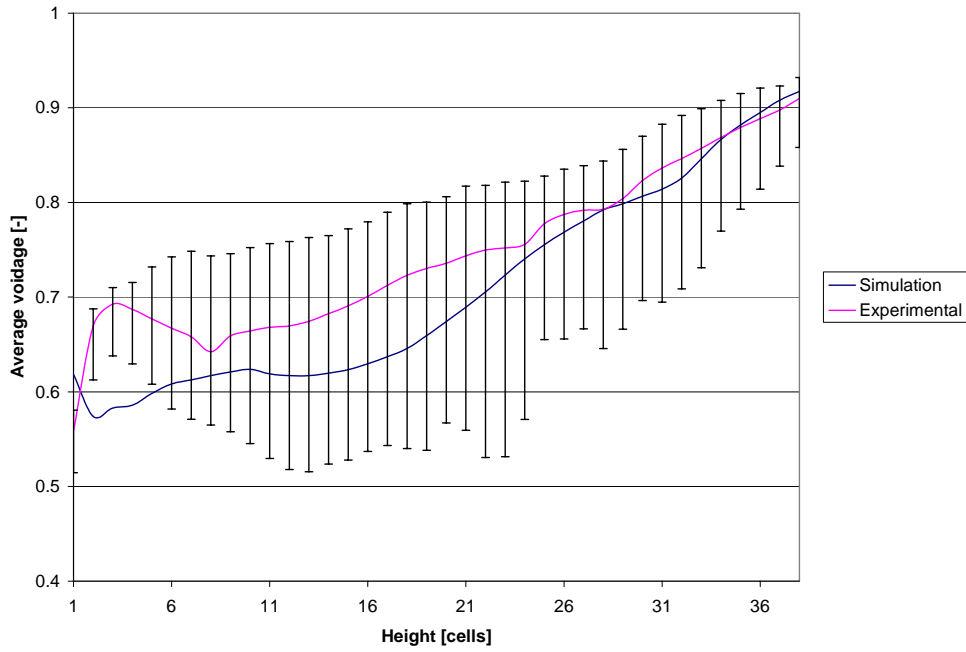


Figure 4: Fluidisation at 2.5 m/s, first experiment

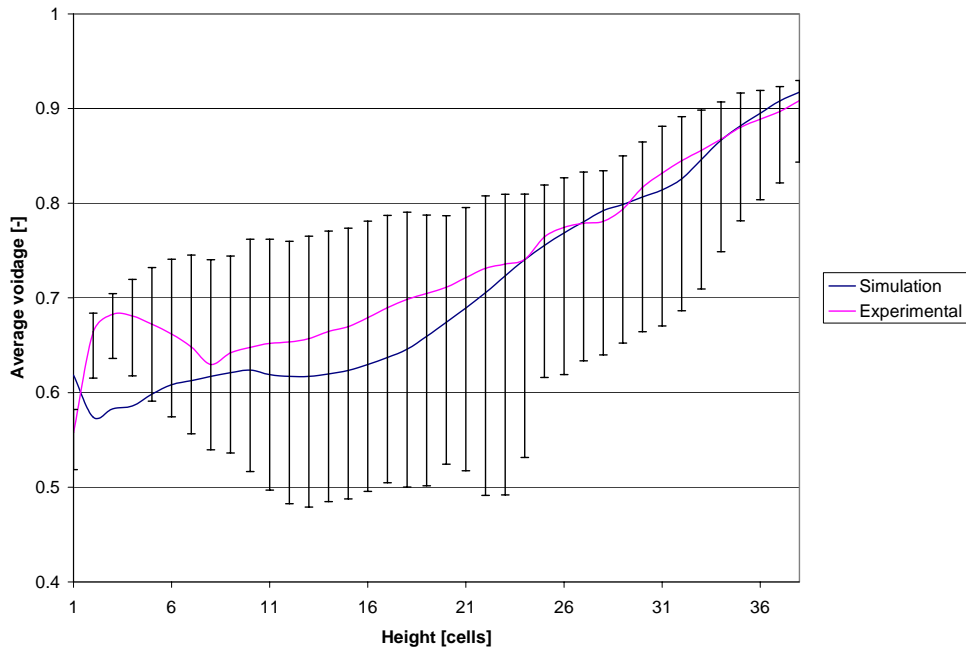


Figure 5: Fluidisation at 2.5 m/s, second experiment

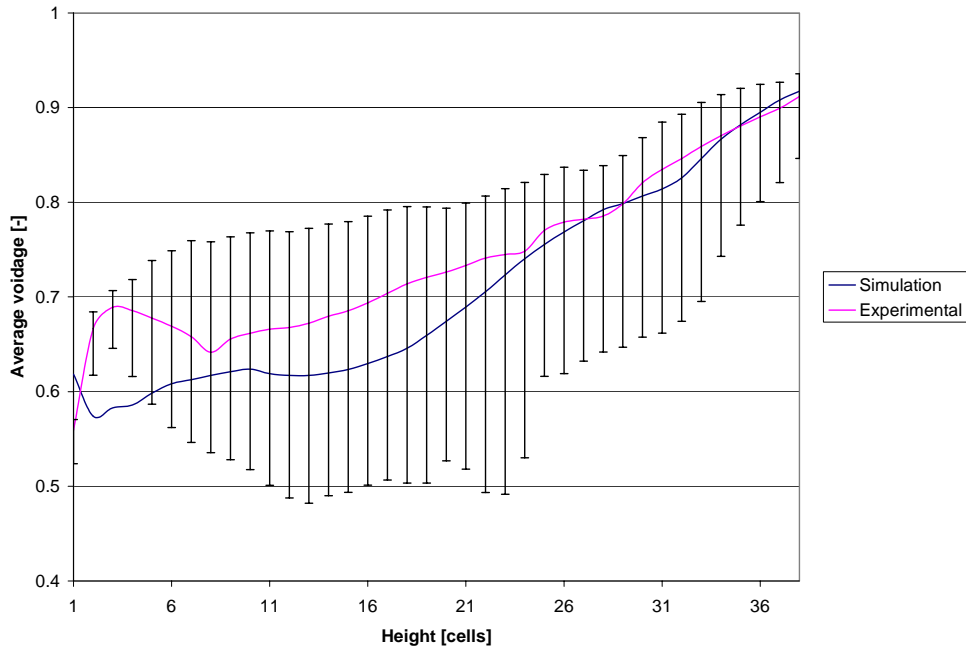


Figure 6: Fluidisation at 2.5 m/s, third experiment

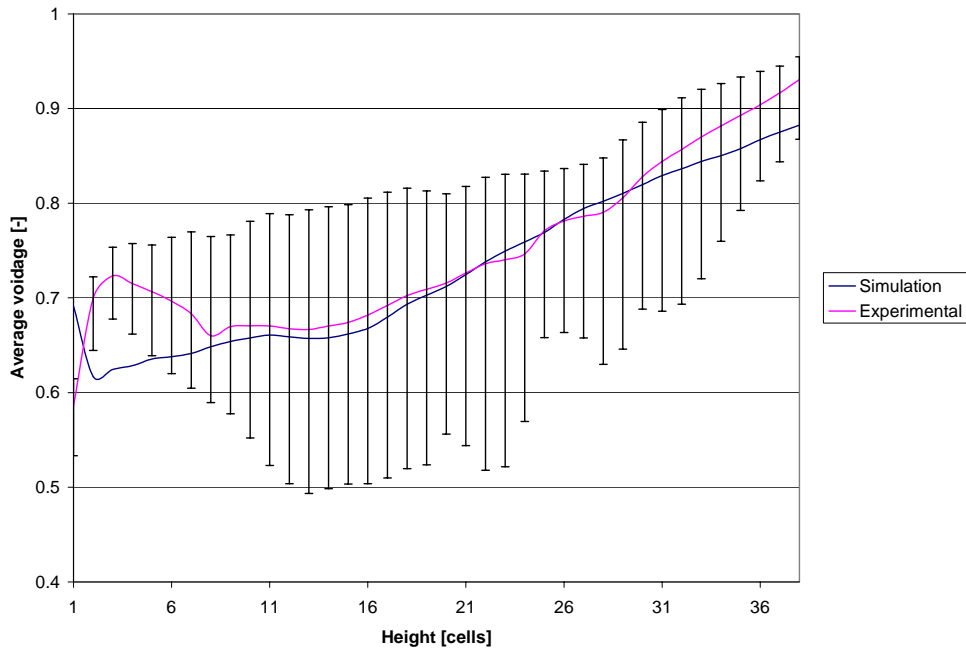


Figure 7: Fluidisation at 3.0 m/s, first experiment

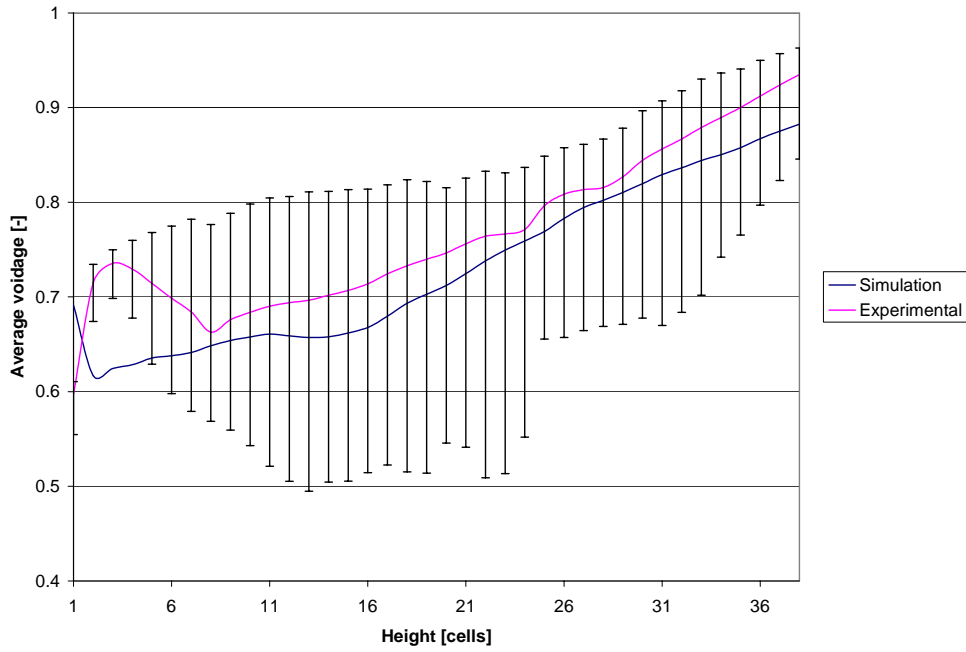


Figure 8: Fluidisation at 3.0 m/s, second experiment

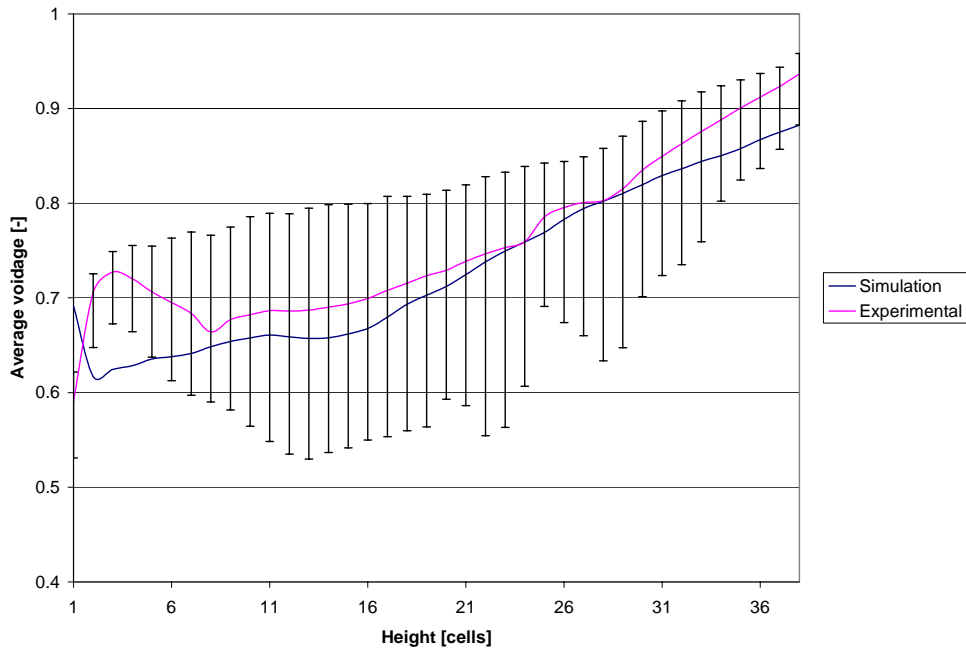


Figure 9: Fluidisation at 3.0 m/s, third experiment

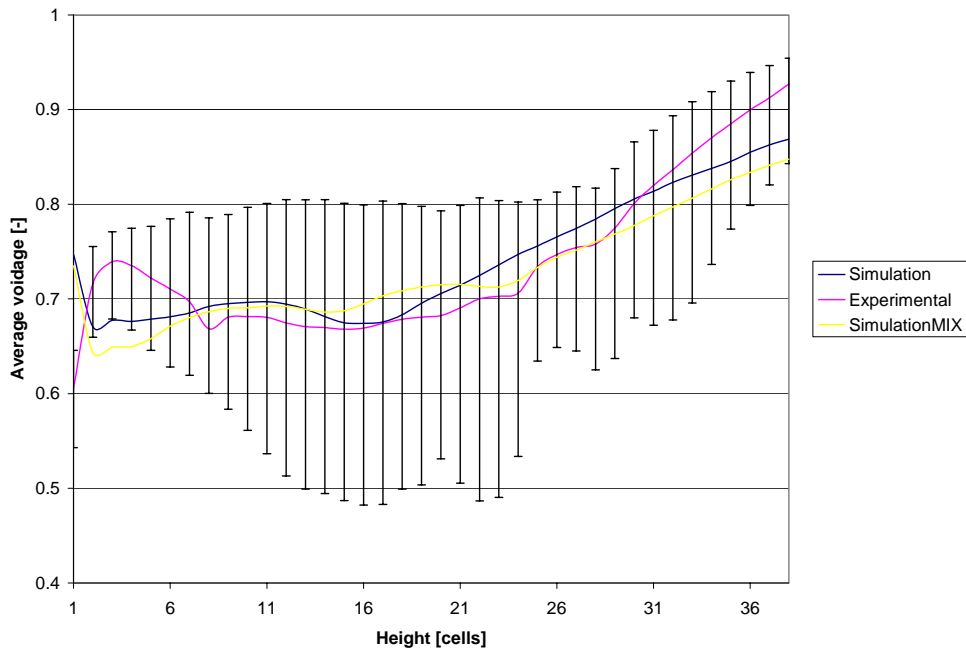


Figure 10: Fluidisation at 3.5 m/s, first experiment

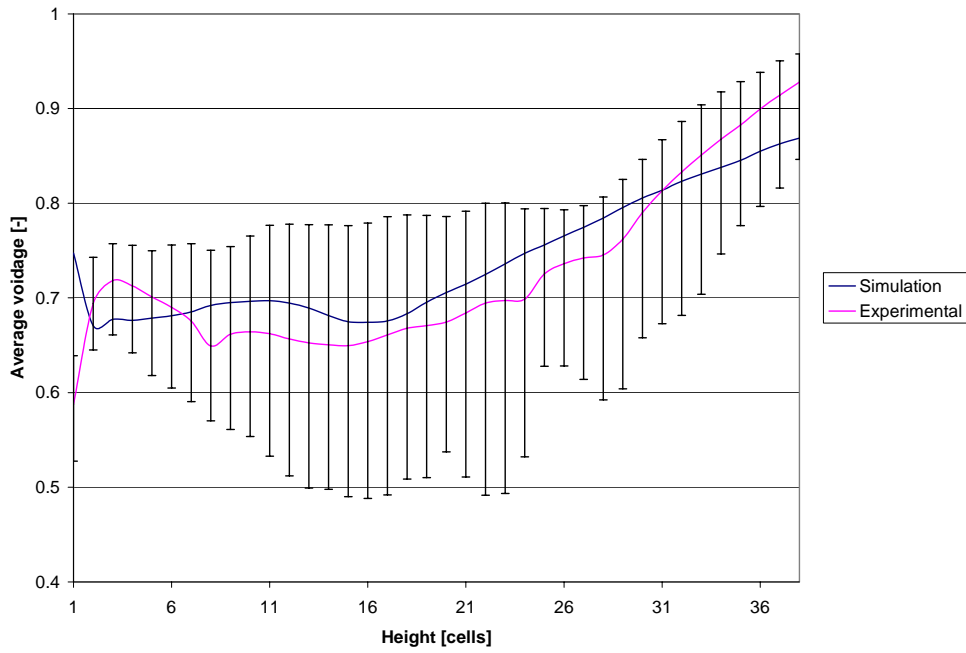


Figure 11: Fluidisation at 3.5 m/s, second experiment

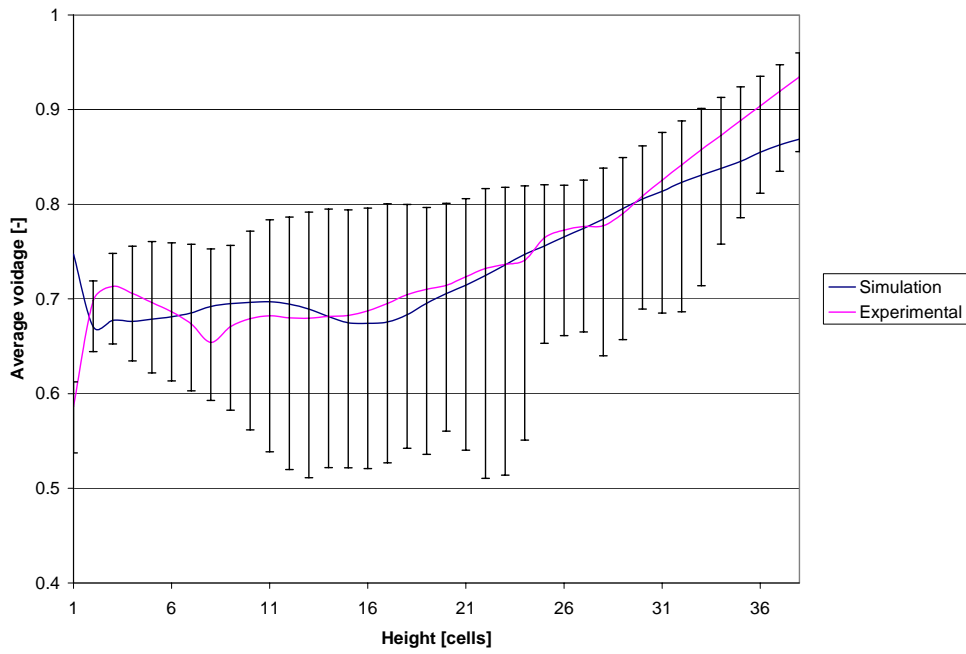


Figure 12: Fluidisation at 3.5 m/s, third experiment

Part 2: Spout-Fluidisation

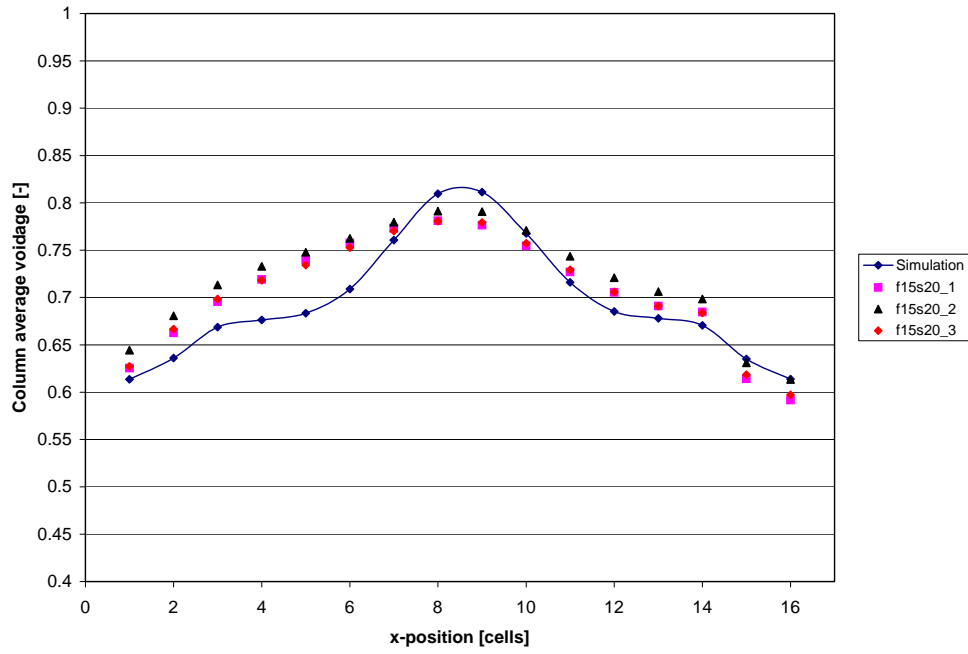


Figure 13: Fluidisation at 1.5 m/s, spout at 20 m/s

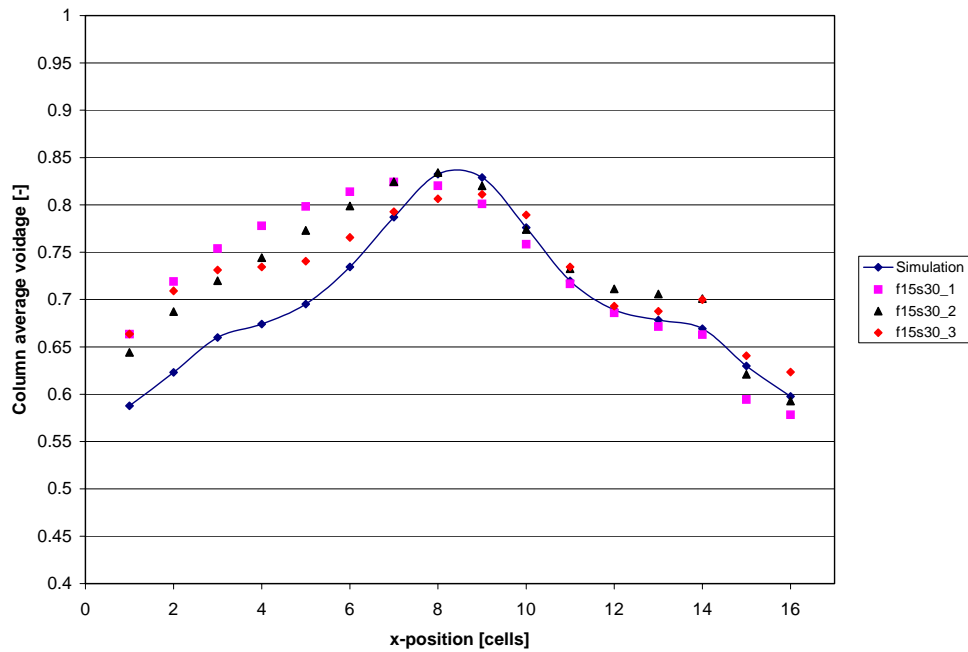


Figure 14: Fluidisation at 1.5 m/s, spout at 30 m/s

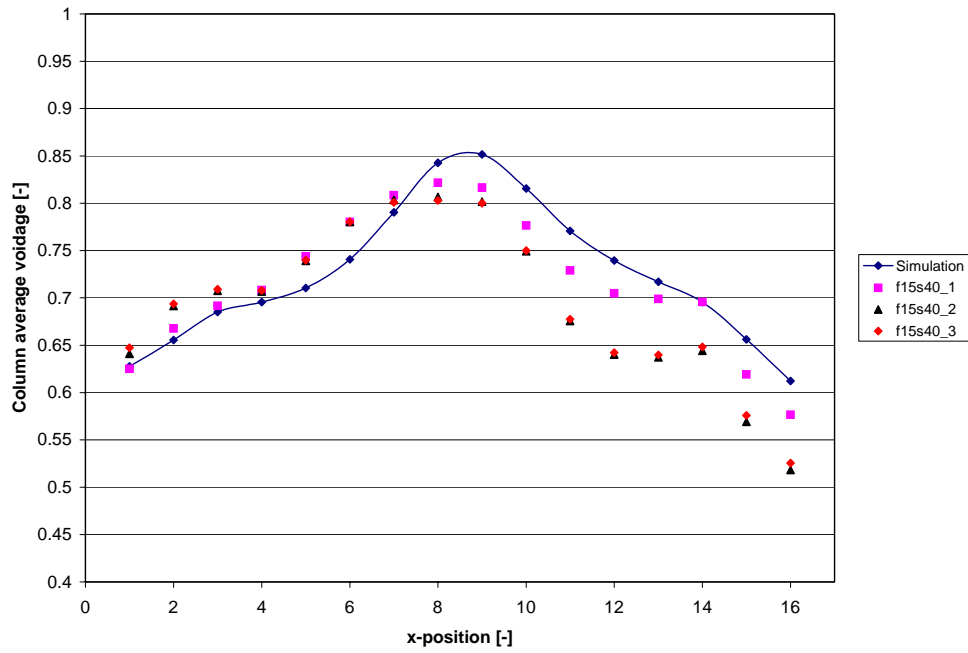


Figure 15: Fluidisation at 1.5 m/s, spout at 40 m/s

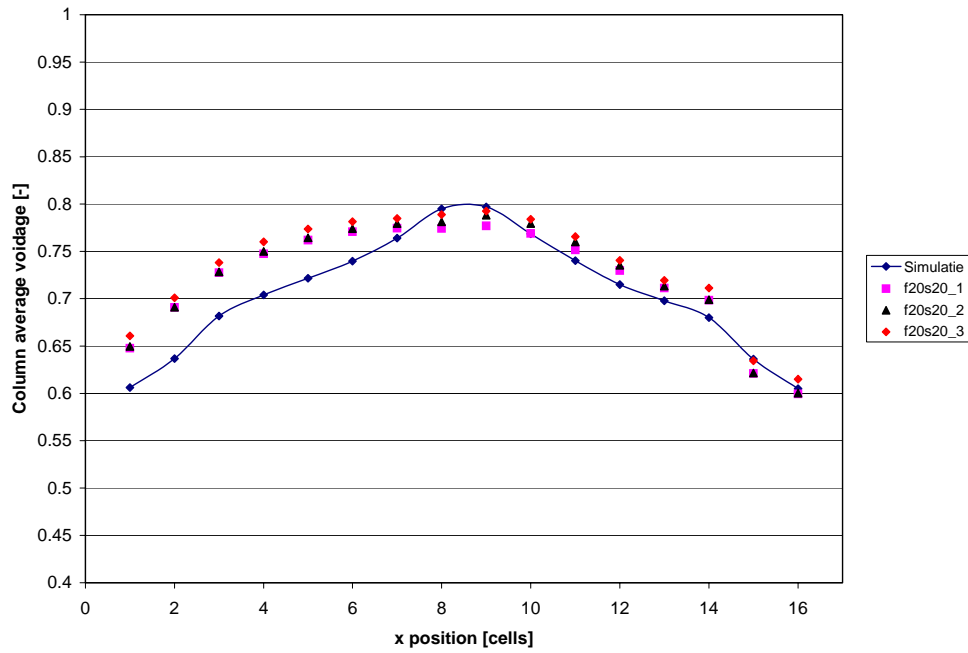


Figure 16: Fluidisation at 2.0 m/s, spout at 20 m/s

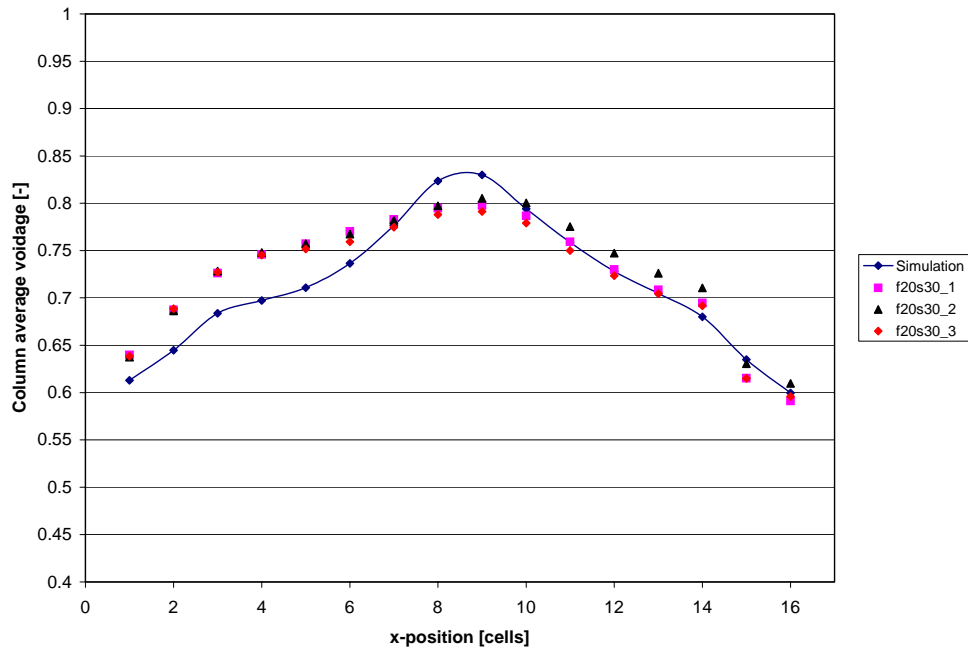


Figure 17: Fluidisation at 2.0 m/s, spout at 30 m/s

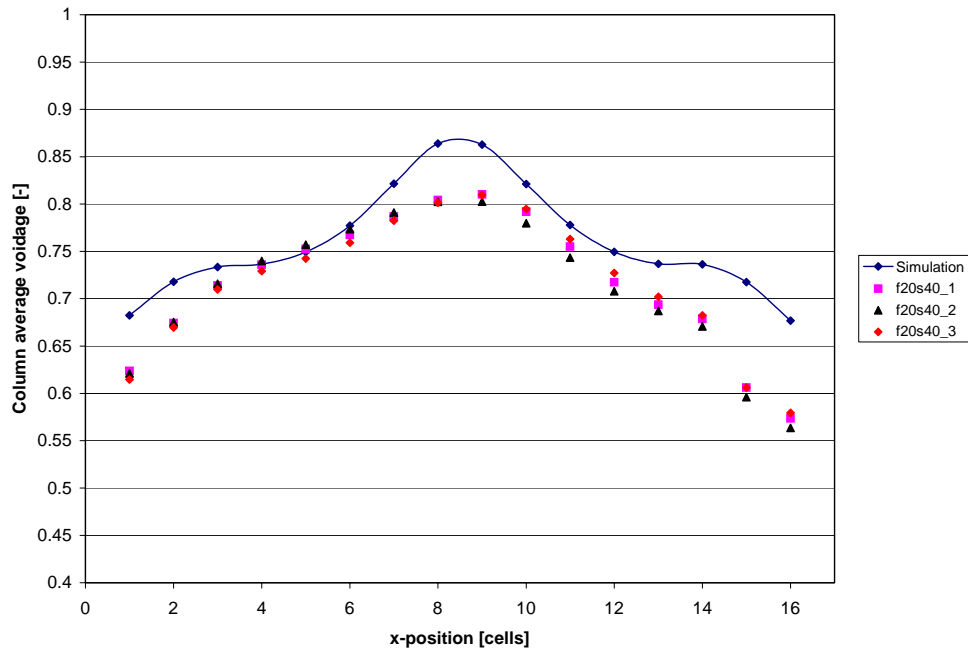


Figure 18: Fluidisation at 2.0 m/s, spout at 40 m/s

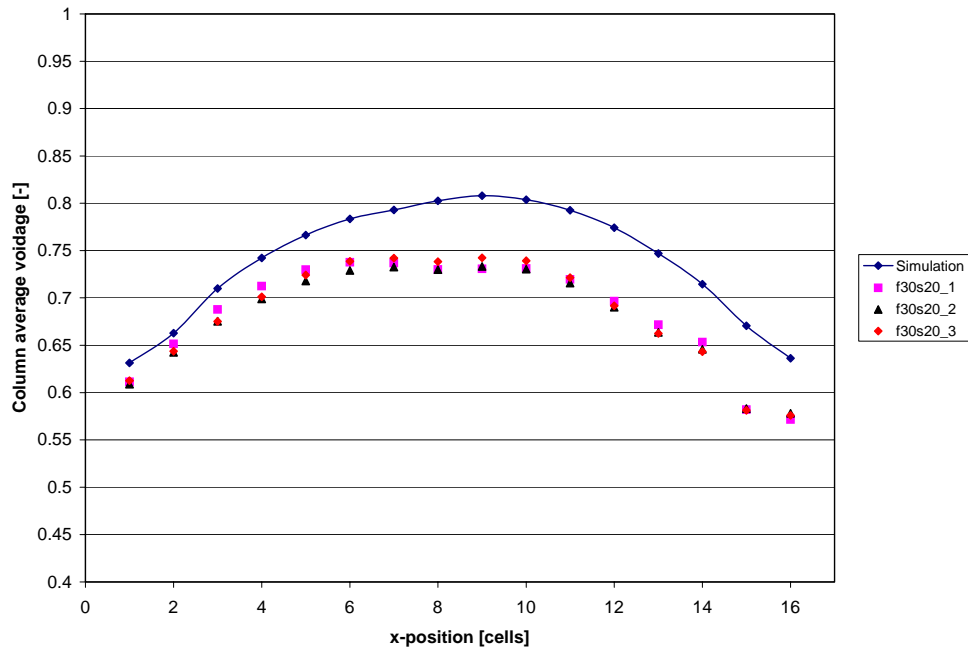


Figure 19: Fluidisation at 3.0 m/s, spout at 20 m/s

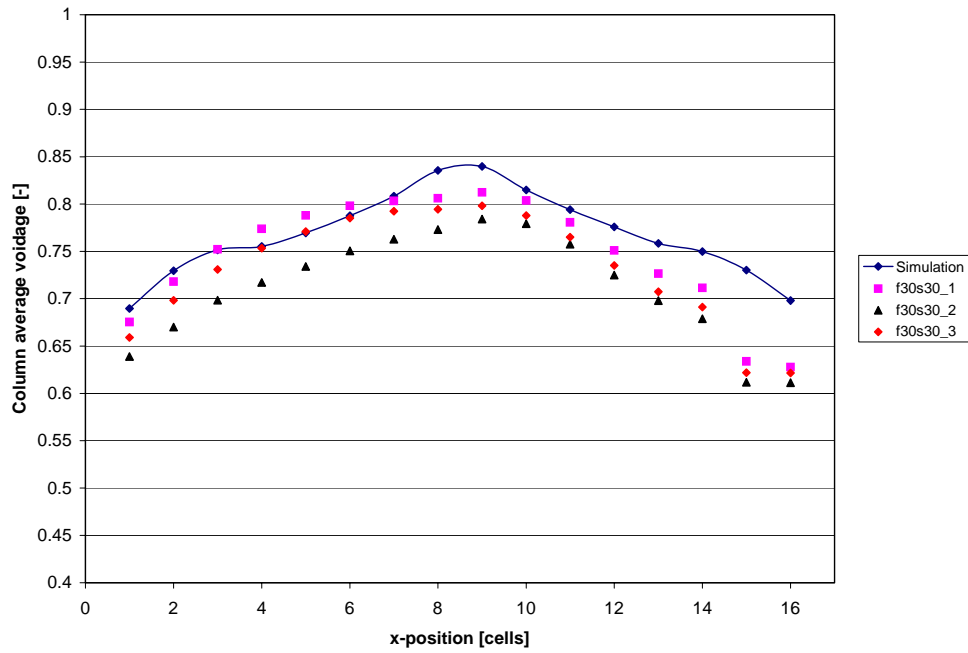
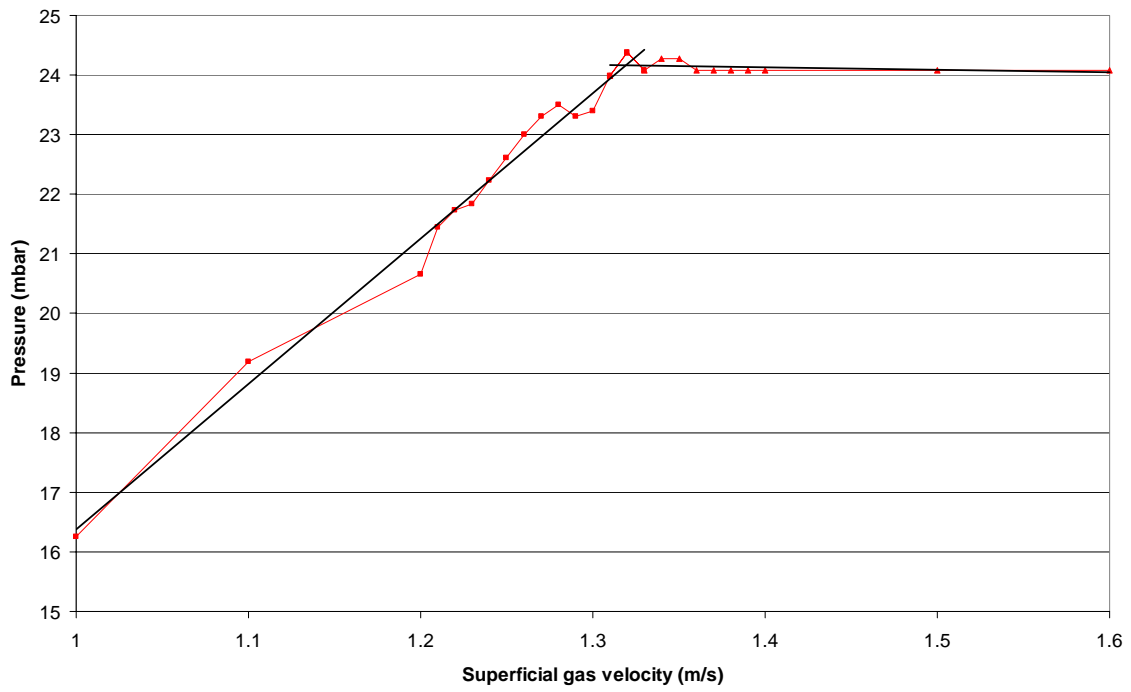


Figure 20: Fluidisation at 3.0 m/s, spout at 30 m/s

Appendix C: Minimum fluidisation



Appendix D: Energy analysis

An energy analysis was performed to determine if a simulation of 32900 red (diameter 2.5 mm) particles gives similar results compared with a simulation of 30000 red and 2900 blue (diameter 3.0 mm) particles.

The energy values in table 1 were obtained from simulations with a duration of 5 seconds. The numbers are the sum of the energies (5000 data points in total) obtained during the simulation.

Fluidisation [m/s]	Sum Kinetic [J]	Sum Rotational [J]	Sum Potential [J]	Total [J]
2.0	302	514	74	890
3.0	898	1250	185	2333
3.5	999	1670	248	2917
3.5 MIX	1150	1710	253	3113
4.0	1170	1690	251	3110

Table 1: Summation of 5000 energies obtained from simulations

If one assumes only a small influence of the mix on the velocities and positions, the energy increase should only be caused by the mass increase since all of the energies depend on the mass in a linear fashion.

$$\text{Kinetic: } U_k = \frac{1}{2} m \mathbf{v}^2$$

$$\text{Rotational: } U_{rot} = \frac{1}{2} I \omega^2, \text{ with } I = \frac{2}{5} m r_p^2$$

$$\text{Potential: } U_{pot} = mgh$$

The increase in mass can be calculated as follows:

32900 red particles: 32900 red particle masses

30000 red particles: 30000 red particle masses

2900 blue particles: $2900 \cdot (3/2.5)^3 = 5011$ red particle masses

Mass increase: $35011/32900 = 1.064$

The mass increase would thus result in a new total energy of $1.064 \cdot 2917 = 3104$ J. The total energy found was 3113 J, so on this basis it can be concluded that the tracer particles do not have a significant influence on velocities and position. The increase was not equal for all types of energy. This could be caused by periodical effects (e.g. bedheight fluctuations) that were not equally taken into account in the simulated time of 5 seconds.

Note must be that taken going from 3.5 m/s to 4.0 m/s, the rotational and potential energy does not significantly increase anymore. However, this energy analysis, combined with a qualitative analysis of the voidage and velocity fields of the mix simulation and its corresponding regular simulation indicates that the results are comparable.

Appendix E: Experimental procedure

Before experiments could be carried out, the temperature of the digital camera and halogen lamps needed to stabilise. This is especially important for the digital camera since the temperature of the CCD chips has a profound effect on the measured colour intensities [22].

After 2 hours of warming, experimentation can begin. First of all, the bed was operated in bubbling mode (gas velocity 2 m/s) and steam is added until static electricity has disappeared. Next:

1. The gas flow is switched of the bed. The pressure probe is positioned. The gas flow is switched to the bed again.
2. Fluidisation and spout velocities are adjusted to the desired velocities. The bed is allowed a few minutes to stabilise.
3. The curtains in the box are all closed. The pressure and image recording are started simultaneously. Experiments have a duration of 30 seconds.
4. For all fluidisation/spout velocities, the experiment is carried out three times. The pressure probe is located on another position for each of the experiments.

The digital camera used a shutter time of 1/500 seconds. An important advantage of the small shutter time is a crisper image; a larger shutter time results in blurring of moving particles.

The frame-grabber can only process a certain amount of data. As a consequence, the quality of the JPEG compression could not be the highest one available. For all experiments a fixed Q factor of 18 and a block size of 508 was used. This value was obtained by recording a vigorously bubbling bed. The Q factor was set on 'auto Q'. With this option enabled, the software automatically determined the correct Q factor. Due to the wild particle movement only a low compression ratio can be reached.

According to Mellema, the compression losses are negligible from a Q factor of 16 and up [22].

Appendix F: Fast Fourier Transform results

Results for an experiment with 2.0 m/s fluidisation:

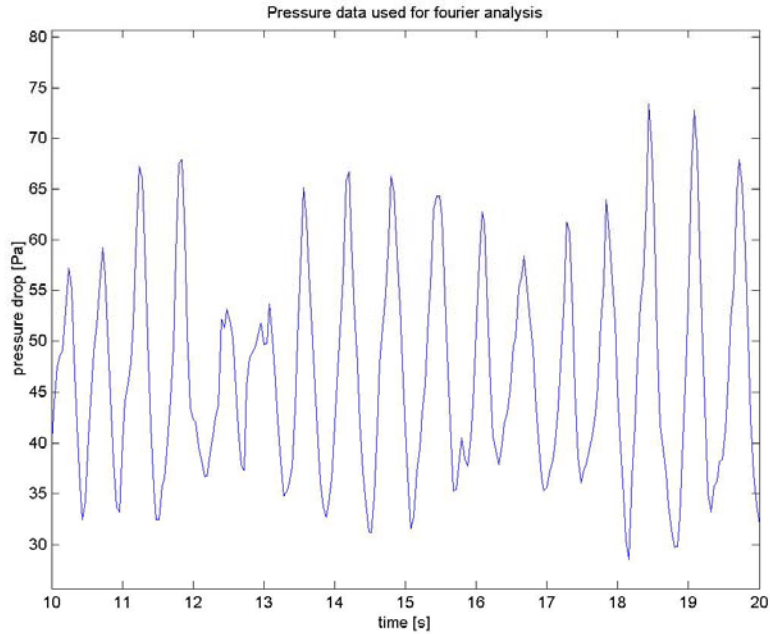


Figure 1: Pressure fluctuations of 2.0 m/s experiment 2

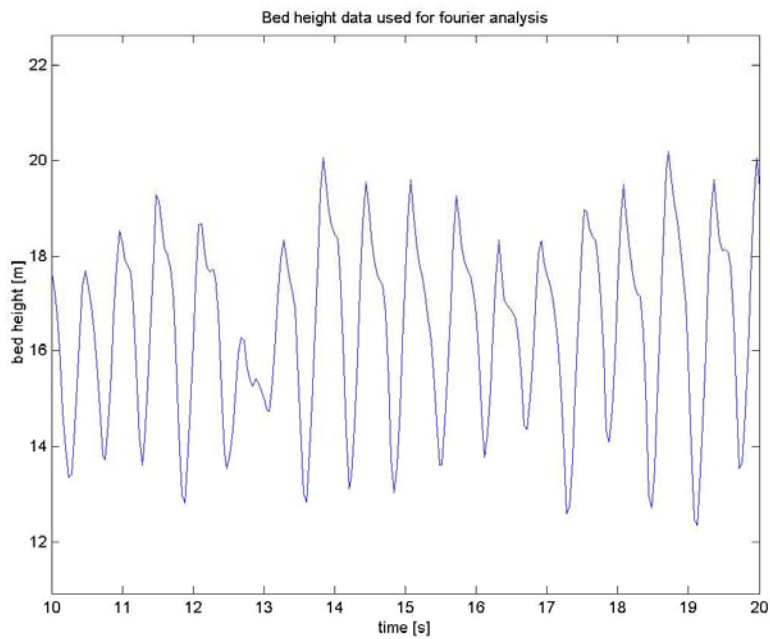


Figure 2: Bedheight fluctuations of 2.0 m/s experiment 2

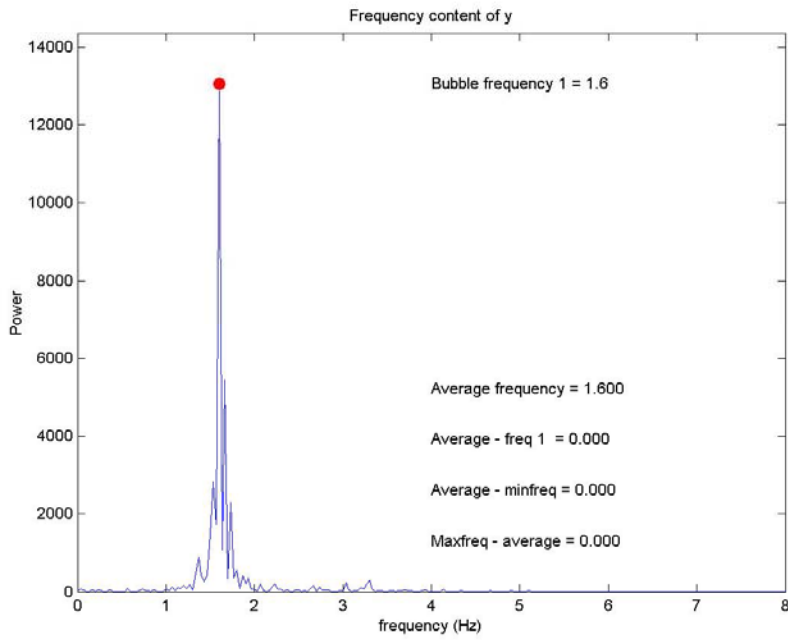


Figure 3: Frequency spectrum on basis of pressure drop fluctuations, experiment 2

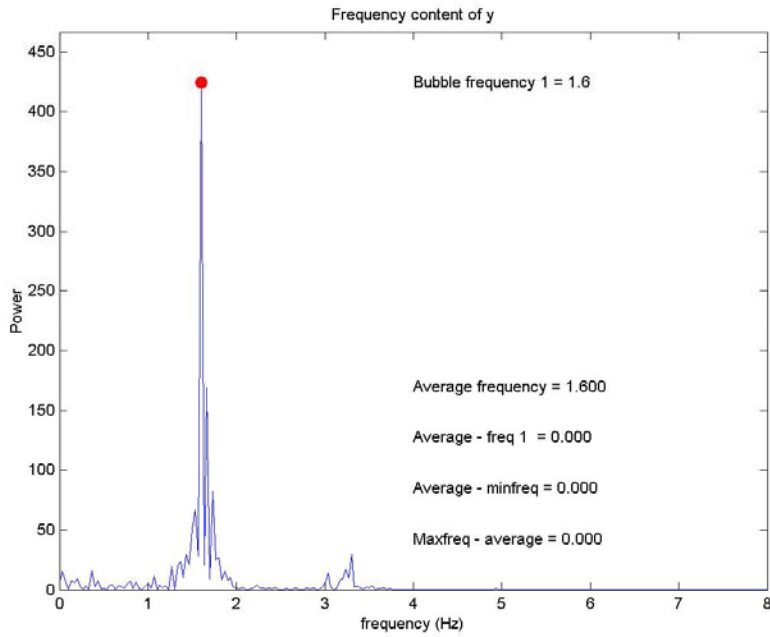


Figure 4: Frequency spectrum on basis of bedheight fluctuations, experiment 2

Appendix G: Relation between RMS and z-coordinate

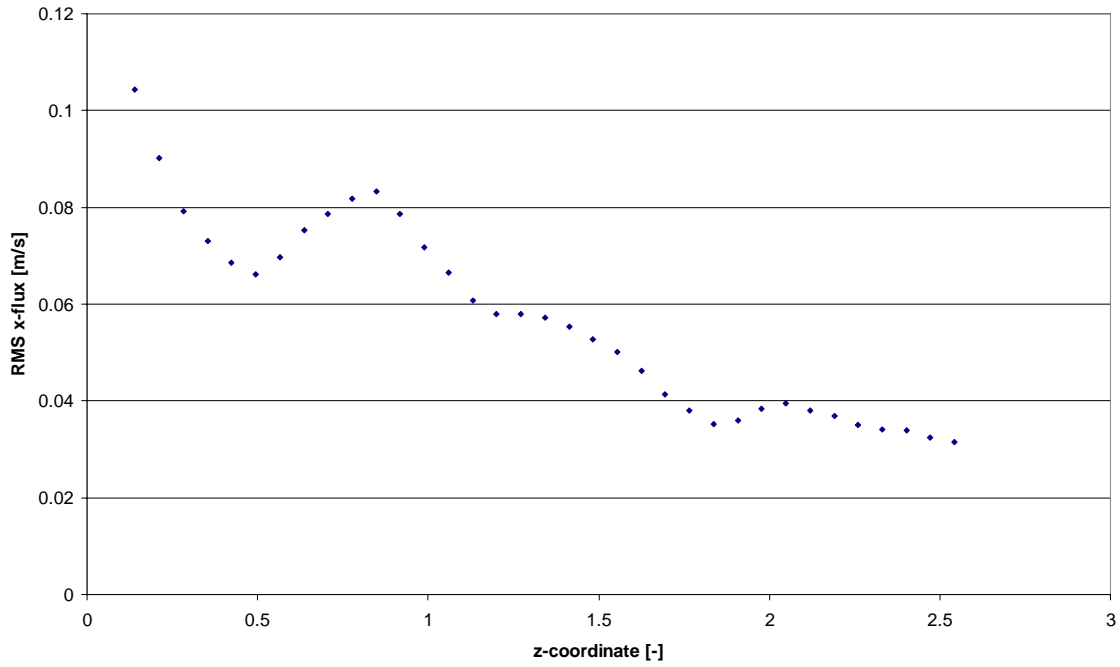


Figure 1: The RMS values of the x-flux, fluidisation at 2.0 m/s, simulation

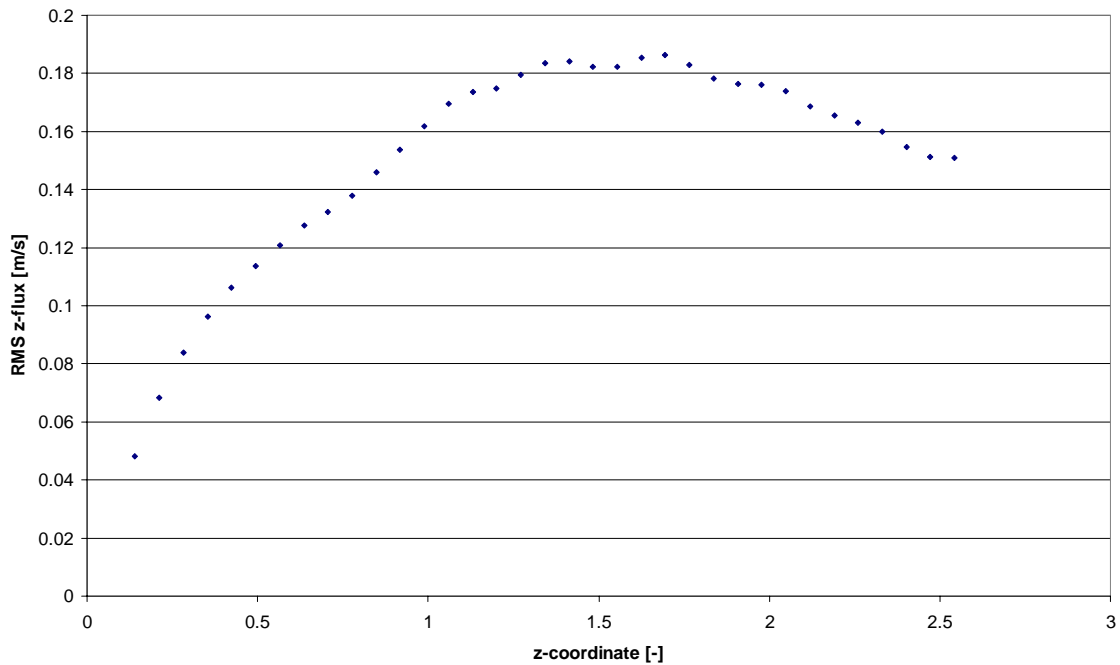


Figure 2: The RMS values of the z-flux, fluidization at 2.0 m/s, simulation